REPORT DOCUMENTATION PAGE

Form Approved
OMB No. 0704-0188

1. REPORT DATE 12 March 2020	**2. REPORT TYPE** Technical Paper	**3. DATES COVERED** *(From - To)* 02 March 2020 - 30 March 2020

4. TITLE AND SUBTITLE
Development of a Normal Shear Stress And Temperature (NSST) Sensor For Solid Rocket Motor Health Monitoring

5a. CONTRACT NUMBER
FA9300-19-C-0003

5b. GRANT NUMBER

5c. PROGRAM ELEMENT NUMBER

6. AUTHOR(S)
James Fillerup and Franklin Wong

5d. PROJECT NUMBER

5e. TASK NUMBER

5f. WORK UNIT NUMBER
Q1Y8

7. PERFORMING ORGANIZATION NAME(S) AND ADDRESS(ES)
Piezo-Metrics Inc. dba Micron Instruments
4509 Runaway St.
Simi Valley, CA 93063

8. PERFORMING ORGANIZATION REPORT NUMBER

9. SPONSORING/MONITORING AGENCY NAME(S) AND ADDRESS(ES)

Air Force Research Laboratory (AFMC)
AFRL/RQRM
4 Draco Drive
Edwards AFB, CA 93524-7160

10. SPONSOR/MONITOR'S ACRONYM(S)

11. SPONSOR/MONITOR'S REPORT NUMBER(S)

AFRL-RQ-ED-TP-2020-073

12. DISTRIBUTION/AVAILABILITY STATEMENT
Distribution Statement A: Approved for Public Release; Distribution is Unlimited. PA Clearance Number: 20125; Clearance Date: 11 March 2020.

13. SUPPLEMENTARY NOTES
The U.S. Government is joint author of the work and has the right to use, modify, reproduce, release, perform, display, or disclose the work.

14. ABSTRACT
Development of shear stress sensors for solid propellant rocket motors was attempted in the early 1970's. The concepts were based on the differential linear displacement between two diagonal line elements that comprised the shear sensor. These sensors needed large strains in the sensing elements to obtain sufficiently high signal-to-noise ratios for the foil strain gages that were used. With the availability of high performance semiconductor strain gages, it may now be possible to design not only a compact shear stress sensor, it may be possible to design a sensor that can simultaneously measure the shear and normal stress components acting on a solid rocket motor bondline. The objective of this study is to numerically determine the potential performance of a diaphragm-based normal shear stress and temperature (NSST) sensor design. The study requires the boundary conditions acting on the sensor to be considered part of the sensor design. The results of the parametric study are presented and discussed. The principal parameters controlling the deformation of the diaphragm under combined stress loading were found to be: 1) the stiffness of the polymer, 2) the loading surface diameter to sensor diameter ratio, 3) the thickness of the polymer on top of the sensor to sensor diameter ratio, 4) the sensor diaphragm diameter, and 5) the sensor diaphragm thickness.

15. SUBJECT TERMS
N/A

16. SECURITY CLASSIFICATION OF:			**17. LIMITATION OF ABSTRACT**	**18. NUMBER OF PAGES**	**19a. NAME OF RESPONSIBLE PERSON**
a. REPORT	**b. ABSTRACT**	**c. THIS PAGE**			James Singleton
					19b. TELEPHONE NUMBER *(Include area code)*
Unclassified	Unclassified	Unclassified	SAR	51	N/A

Standard Form 298 (Rev. 8/98)
Prescribed by ANSI Std. Z39.18

DEVELOPMENT OF A NORMAL SHEAR STRESS AND TEMPERATURE (NSST) SENSOR FOR SOLID ROCKET MOTOR HEALTH MONITORING

Finite Element Analysis and Data Reduction

JM Fillerup
FC Wong
Micron Instruments
4509 Runaway St.
Simi Valley, CA 93063

February 2020

Terms of Release: Distribution Statement A: Approved for Public Release; Distribution is Unlimited. PA# 20125

Micron Instruments
Contract Report
Micron CR 2020-001

This work was performed at Micron Instruments between April 2019 and December 2019 for Contract FA9300-19-C-0003, Subtopic 5 Sensor Technology Development for Solid Rocket Motors under Broad Agency Announcement Motor Aging and Surveillance Technology (BAA MAST) Call 3 (BAA-RQR-2014-0002) Aging and Surveillance (A&S) Technology Development.

Abstract

Development of shear stress sensors for solid propellant rocket motors was attempted in the early 1970's. The concepts were based on the differential linear displacement between two diagonal line elements that comprised the shear sensor. These sensors needed large strains in the sensing elements to obtain sufficiently high signal-to-noise ratios for the foil strain gages that were used. With the availability of high performance semiconductor strain gages, it may now be possible to design not only a compact shear stress sensor, it may be possible to design a sensor that can simultaneously measure the shear and normal stress components acting on a solid rocket motor bondline. The objective of this study is to numerically determine the potential performance of a diaphragm-based normal shear stress and temperature (NSST) sensor design. The study requires the boundary conditions acting on the sensor to be considered part of the sensor design. The results of the parametric study are presented and discussed. The principal parameters controlling the deformation of the diaphragm under combined stress loading were found to be: 1) the stiffness of the polymer, 2) the loading surface diameter to sensor diameter ratio, 3) the thickness of the polymer on top of the sensor to sensor diameter ratio, 4) the sensor diaphragm diameter, and 5) the sensor diaphragm thickness.

Table of contents

List of Figures

List of Tables

Acknowledgements

The authors would like to acknowledge the support from James Singleton, Group Lead – SRM Aging and Surveillance, Solid Rocket Motors Branch, AFRL Aerospace Systems Directorate, Edwards AFB.

1. INTRODUCTION

Failure at the propellant-to-liner or liner-to-case interface at or near the stress relief termination is one of the major failure modes in a solid propellant rocket motor [1]. Numerical methods and polymeric material characterization techniques have been developed to handle stress singularities and nonlinear behavior. The presence of intentional and non-intentional material discontinuities, irregular component geometries and material variability, though, makes numerical assessment of the stress state in a production motor more complicated. Instrumenting all or a sample of motors with normal-shear stress sensors would allow the bondline stress state to be measured in critical, high risk areas thereby increasing confidence that the stress state acting on the bondline is known. Both these items are important for accurate determination of the remaining rocket motor service life.

The Micron Dual Bond Stress and Temperature (DBST) sensor incorporates design features and manufacturing standards in the sensor body that minimize material creep and environmental degradation that can lead to sensor output instability over the life of a solid rocket motor (SRM). Micron has demonstrated the DBST sensor's ability to measure stress and temperature within power limits that prevent unintended propellant ignition. Hence, Micron believes the DBST sensor design has the basic stability to safely measure the stresses at the propellant-liner-interface over the anticipated service life of a strategic asset.

Micron is modifying the diaphragm sensor concept to allow shear stress measurement as well as normal stress measurement. The diaphragm concept is being pursued, as opposed to the other concepts, because it is a structurally simpler method to simultaneously measure normal and shear stress-generated deformations when high gage factor semiconductor strain gages, such as those produced by Micron Instruments, are used.

The overall objective of the development project is to design, fabricate, calibrate and validate the performance of a normal-shear stress sensor capable of measuring normal bondline stress, bondline shear stress and temperature (NSST) in a solid rocket motor.

This report documents the theoretical analyses that support the NSST design and the proposed data reduction method. Section 2 summarizes some of the past efforts to design normal and shear stress sensors. Section 3 describes the finite element model of the proposed sensor and the details of the model boundary conditions. Section 4 presents the parametric study that determines the required specimen geometry needed for calibration of the NSST sensor. Section 5 discusses the selection of gage placement locations that allow simultaneous measurement of normal and shear stresses and presents the method to reduce the strain data to obtain the normal and shear stress magnitudes acting on a case-propellant interface.

2. BACKGROUND

The development of normal stress sensors traces its history back to the mid-1970’s [2]. At the time, pressure transducers were modified to measure the normal bond stress levels generated by solid propellants. The modifications were not very successful because the foil strain gages used in the transducers required a thin metal diaphragm to have an acceptable signal-to-noise ratio. However, a thin diaphragm would deform differently for the same loading condition depending on the temperature-dependent modulus of the propellant. Improvements to bond stress sensor accuracy was made by introducing the use of semiconductor strain gages [3]. The higher gage factor of the semiconductor strain gage allowed thicker diaphragm designs while maintaining good signal-to-noise characteristics. The use of semiconductor strain gages also allowed the size of the sensor to become smaller and less intrusive in the propellant stress field. As development continued to the mid-2010’s, Micron Instruments refined the sensor design, material selection and manufacturing process to mitigate the major contributors to sensor instability [4]. Data collected over a fifteen year period indicated that the DBST should possess low drift characteristics that would make it useful for evaluating the stress-state of a solid rocket motor over a thirty year period. From the safety point of view, in-house tests showed that the DBST failed in a safe manner without sparking or overheating from over-voltages, over-currents or shorts. Hence, no unintended propellant ignition should occur if the DBST experiences an electrical failure [5], [6].

In the latter part of the 1980’s [7], the concept of a shear stress sensor was proposed. It was recognized that the stress state at the case-propellant interface in the transition region of a solid rocket motor was complex and that a normal stress sensor would only reveal a partial picture of the total stress state. Industry was funded to develop and evaluate different concepts to measure shear stress at a motor bondline [8]. Five concepts were produced with sensing elements ranging from beams, wedges and diaphragms.

3. FINITE ELEMENT MODEL

The Micron DBST currently incorporates one strain gage bridge to measure diaphragm deformations corresponding to normal stresses. Micron proposes that an additional strain gage bridge be incorporated onto the sensor diaphragm to simultaneously measure deformations related to shear stress. The shear stress sensor design is developed using the linear elastic finite element analysis (FEA) method. ANSYS Mechanical was used as the FEA modeling tool [9].

3.1 Model Geometry

The starting point for the finite element analysis leverages off the work done by AMRDEC in 2006 to model a bond strength test specimen [10]. Schematics of the AMRDEC general model and the Micron ANSYS bond stress model are shown in Figure 1. The geometries are representative of a calibration fixture that will reproduce the normal and shear stress conditions found in a typical axisymmetric solid rocket motor. The primary difference between the two models is the mounting of the sensor. In the AMRDEC model, the sensor is mounted on the grip or endtab. In the Micron ANSYS model, the sensor is embedded in the grip/endtab. By embedding the sensor in the endtab any potential stress perturbations around the sensor body are eliminated.

A no-rotation constraint is imposed on the top endtab. Thus, the top endtab always remains parallel to the lower endtab no matter what forces are applied to the top endtab.

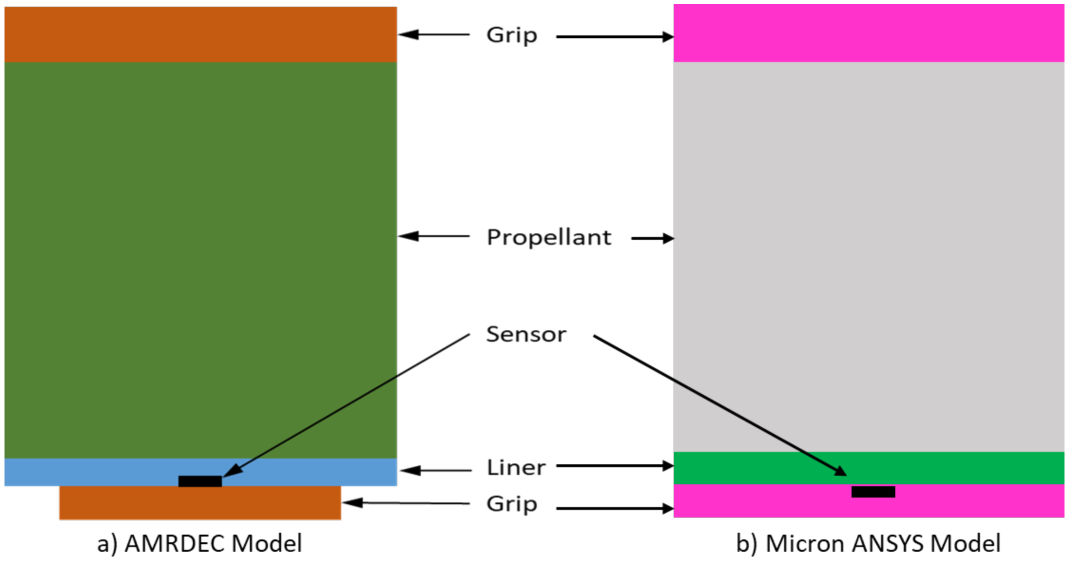

Figure 1: Schematic of General Finite Element Models for the Calibration Fixture

3.2 Material Properties

The mechanical properties of the materials used in the parametric studies are shown in Table 1. The first parametric study considered the effect of propellant and liner moduli on the sensor diaphragm deformation. The range of moduli was varied between 100 (1 E2) psi to 1,000,000 (1 E6) psi. Figure 2 shows the finite element mesh and the boundary conditions used in study.

Table 1. Mechanical Properties of Materials in Calibration Fixture

	Elastic Modulus E, psi	**Poisson's Ratio ν**	**Coefficient of Thermal Expansion CTE, °F^{-1}**
Grips (Aluminum)	10.4 E6	0.32	13 E-6
Polymer	Study Range 1 E2 to1 E6	0.495	47.5 E-6
Liner	Study Range 1 E2 to1 E6	0.495	47.5 E-6
Baseline Polymer Modulus	1000 (1 E3)	0.495	47.5 E-6
Sensor (Titanium)	16.6 E6	0.34	6.8 E-6
Case (Aluminum)	10.4 E6	0.32	13 E-6

The results of the modulus study show that the diaphragm deformation is insensitive to either the polymer or liner moduli for values less than 3,200 psi (see Figure 3). Since both polymer and liner moduli are within this range (i.e. E < 3200 psi) for typical storage and most operating conditions, an arbitrary baseline value of 1000 psi was selected for the remainder of the parametric studies for easy scalability. For future reference, the baseline modulus will be referred to as the 'polymer' modulus, E_poly=1000 psi. Should E_poly be greater than 3,200 psi, the sensor calibration process would need to account for the load carrying effect of the polymer above the diaphragm.

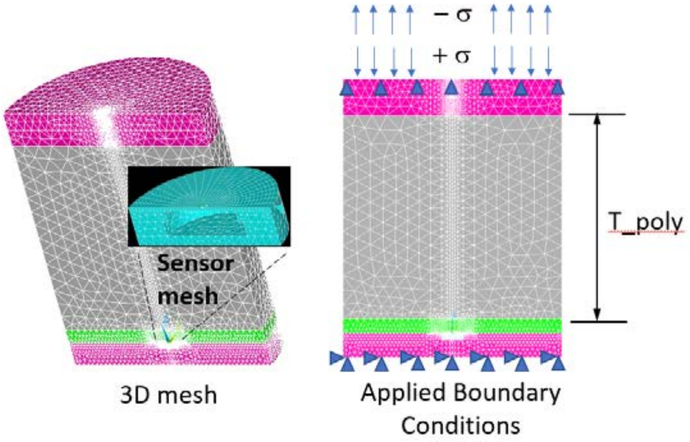

Parameter	Values
D_sens (in.)	0.300
D_tab (in)	3.0
T_prop (in)	2.8
T_liner (in)	0.2
σ (psi)	±50
D_diap (in.)	0.150
T_diap (in.)	0.0075
E_sens (psi)	16.6e6
E_prop/liner (psi)	1.0e (1, 2, 3, 4, 5, 6)
E_tab (psi)	10.4e6

Figure 2: Model Parameters and Boundary Conditions

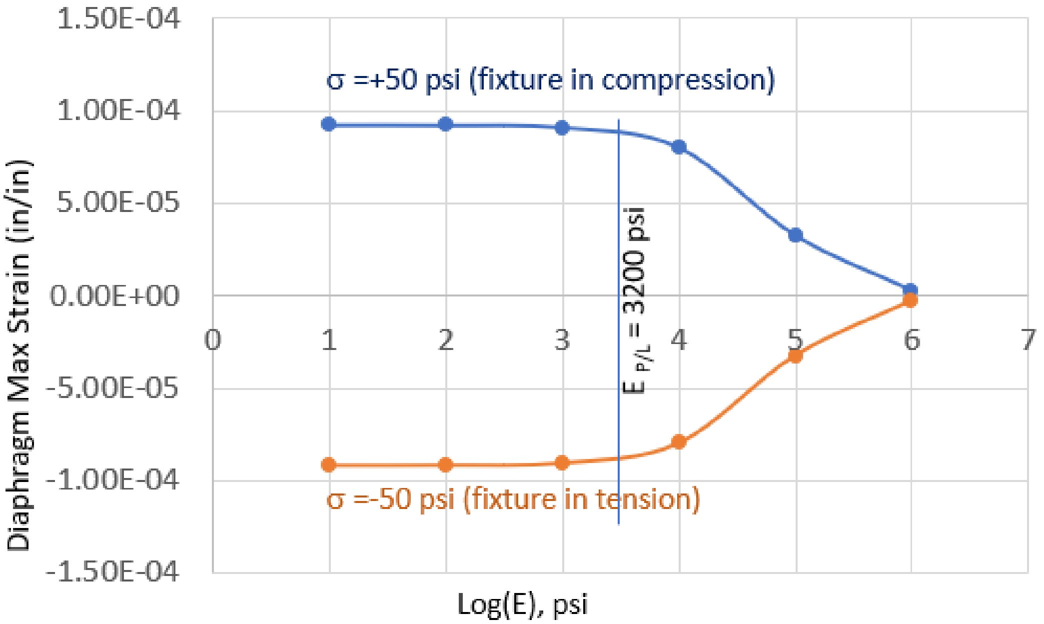

Figure 3: Effects of Polymer Modulus on the Diaphragm Response

4. PARAMETRIC STUDY OF THE CALIBRATION FIXTURE GEOMETRY

The geometry of the calibration fixture plays a major role in how the sensor diaphragm responds to an applied load (see Figure 4). Parametric studies were conducted to consider the geometric effects of: 1) the endtab diameter-to-sensor diameter ratio (D_tab/D_sens), 2) the thickness of the polymer-to-endtab ratio (T_poly/D_tab), 3) the load angle (σ_angle) applied to the top endtab, and 4) the diameter to thickness ratio (D_diap/T_diap) of the diaphragm. These parameters are highlighted in red in the Table found in Figure 4. The sensor diameter, D_sens, was kept at a constant 0.30 in. An equivalent force corresponding to a pressure load of 50 psi, was applied to the top endtab (i.e. $F = \sigma \pi (D\_tab/2)^2$). Since symmetry was used in the FEA model, the actual load applied to the model was F/2.

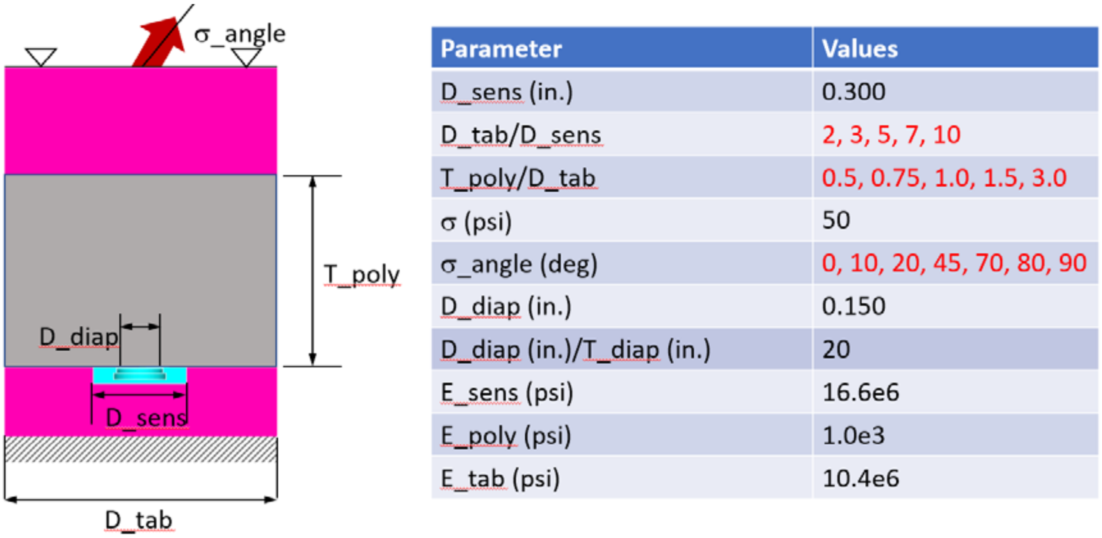

Parameter	Values
D_sens (in.)	0.300
D_tab/D_sens	2, 3, 5, 7, 10
T_poly/D_tab	0.5, 0.75, 1.0, 1.5, 3.0
σ (psi)	50
σ_angle (deg)	0, 10, 20, 45, 70, 80, 90
D_diap (in.)	0.150
D_diap (in.)/T_diap (in.)	20
E_sens (psi)	16.6e6
E_poly (psi)	1.0e3
E_tab (psi)	10.4e6

Figure 4: Parameters of Calibration Geometry Studies.

4.1 Effect of Fixture Diameter and Height

A series parametric, finite element analyses were conducted to considered the diaphragm response for various calibration fixture geometries in shear (i.e., σ_angle = 0 deg). Table 2 shows the matrix of T_poly/T_tab vs. D_tab/D_sens ratios analyzed.

Table 2. Parametric Matrix used for Calibration Fixture Geometry Study

	D_tab/D_sens				
T_poly/T_tab	**2**	**3**	**5**	**7**	**10**
0.5		X			X
0.75		X			X
1.00	X	X	X	X	X
1.50		X			X
2.00		X			X
σ_angle = 0 deg E_poly = 1000 psi D_sens = 0.3 in. Equivalent 50 psi load applied to the top of the endtab.					

The analysis results are presented in a series graphs which correspond to the radial strains along the plot path as illustrated in Figure 5. The Figure shows the plot path as a yellow dashed line along the bottom surface of the diaphragm. The origin of the plot path, DIST = 0, is on the left side of the diaphragm and increases along the diaphragm diameter to the right side at DIST = 0.15 inches. The center of the diaphragm is at DIST = 0.075 in.

Both radial and hoop strains play a role in understanding the diaphragm behavior. However, radial strain is the primary quantity of interest because it will be measured by the strain gages that are bonded onto the diaphragm. The strain gage placement and Wheatstone bridge design are discussed in Section 5.

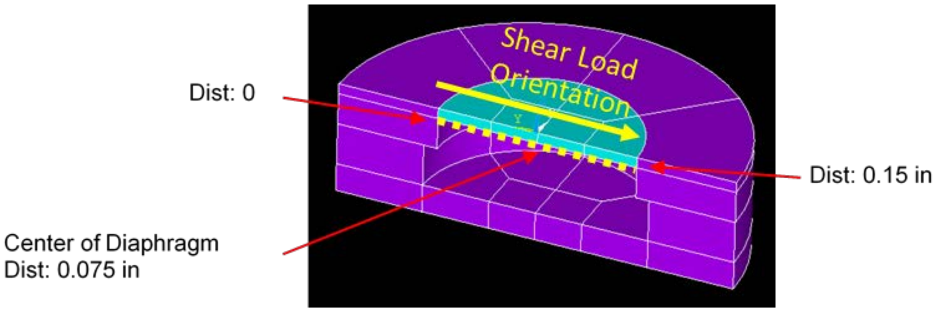

Figure 5: Plot Path on Sensor Diaphragm used for Results Reporting

Referring to the parametric matrix in Table 2, Figures 6 to11 show the FEA models and the corresponding radial strain plots for the analyses performed.

Figure 6 shows the models and the relative geometries for D_tab/D_sens = 3 and T_poly/D_tab ratios = 0.5, 0.75, 1.0, 1.5, 2.0 which study the effects of polymer thickness. Figure 7 shows the resulting Radial Strains vs Plot Path – DIST for each geometry.

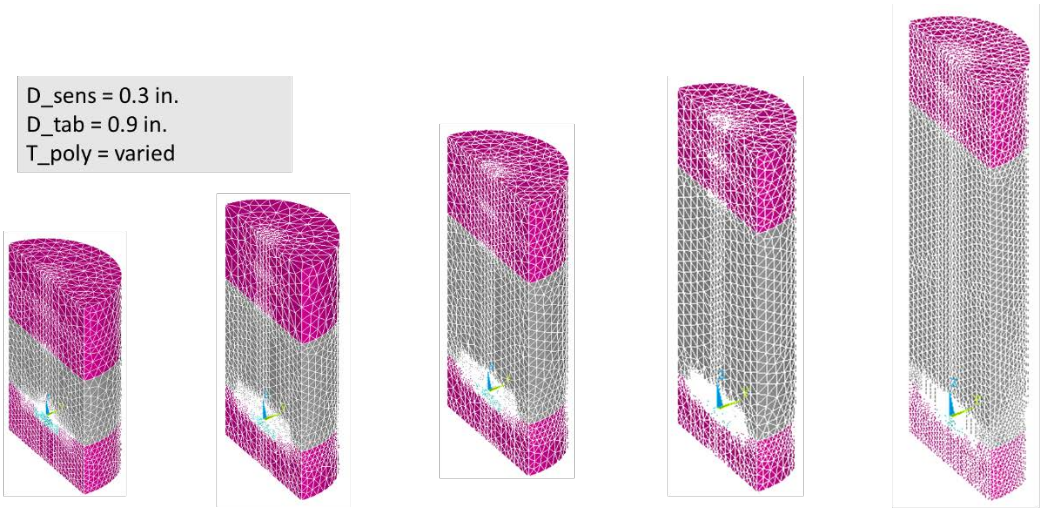

D_tab/D_sens = 3
T_poly/D_tab = 0.5

D_tab/D_sens = 3
T_poly/D_tab = 0.75

D_tab/D_sens = 3
T_poly/D_tab = 1.0

D_tab/D_sens = 3
T_poly/D_tab = 1.5

D_tab/D_sens = 3
T_poly/D_tab = 2.0

Figure 6: Parametric Models for D_tab/D_sens = 3; T_poly/D_Tab varied

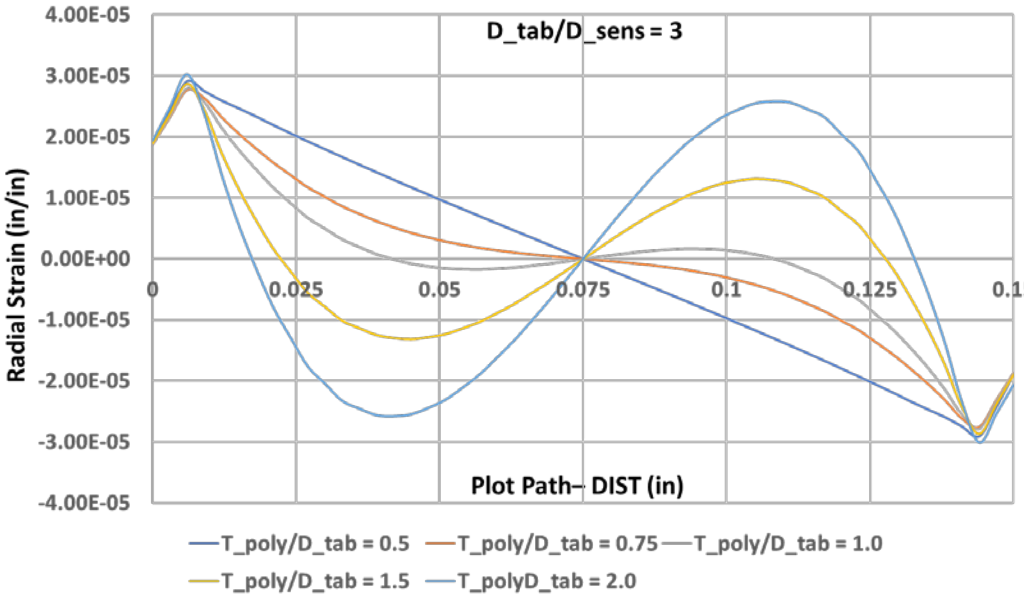

Figure 7: Radial Strain vs DIST for D_tab/D_sens = 3; T_poly/D_Tab varied

Figure 8 shows the models for D_tab/D_sens = 10 and T_poly/D_tab ratios = 0.5, 0.75, 1.0, 1.5, 2.0 with their resulting Radial Strains vs Plot Path – DIST plots provided in Figure 9. This series of analyses likewise studied the effects of polymer thickness, but also considered the effects of a larger endtab diameter.

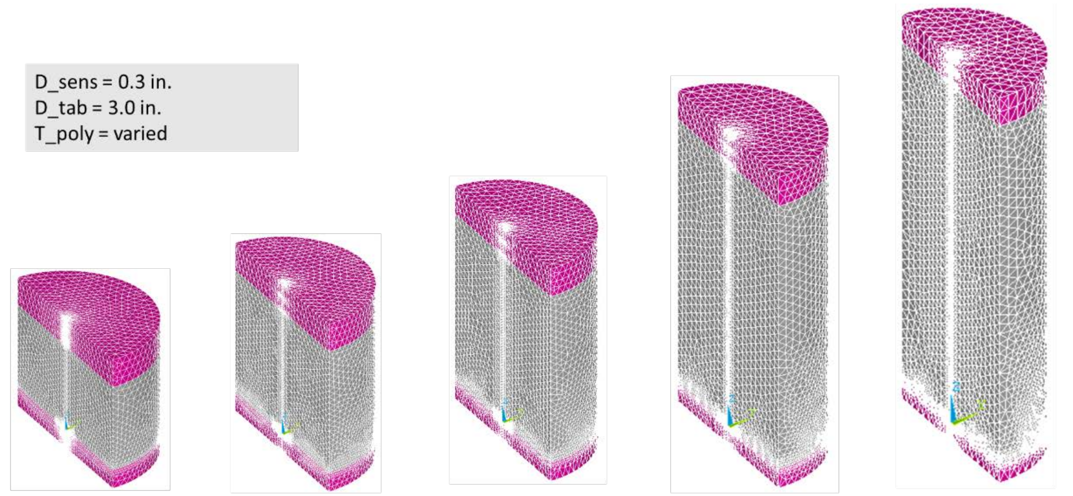

D_tab/D_sens = 10
T_poly/D_tab = 0.5

D_tab/D_sens = 10
T_poly/D_tab = 0.75

D_tab/D_sens = 10
T_poly/D_tab = 1.0

D_tab/D_sens = 10
T_poly/D_tab = 1.5

D_tab/D_sens = 10
T_poly/D_tab = 2.0

Figure 8: Parametric Models for D_tab/D_sens = 10; T_poly/D_Tab varied

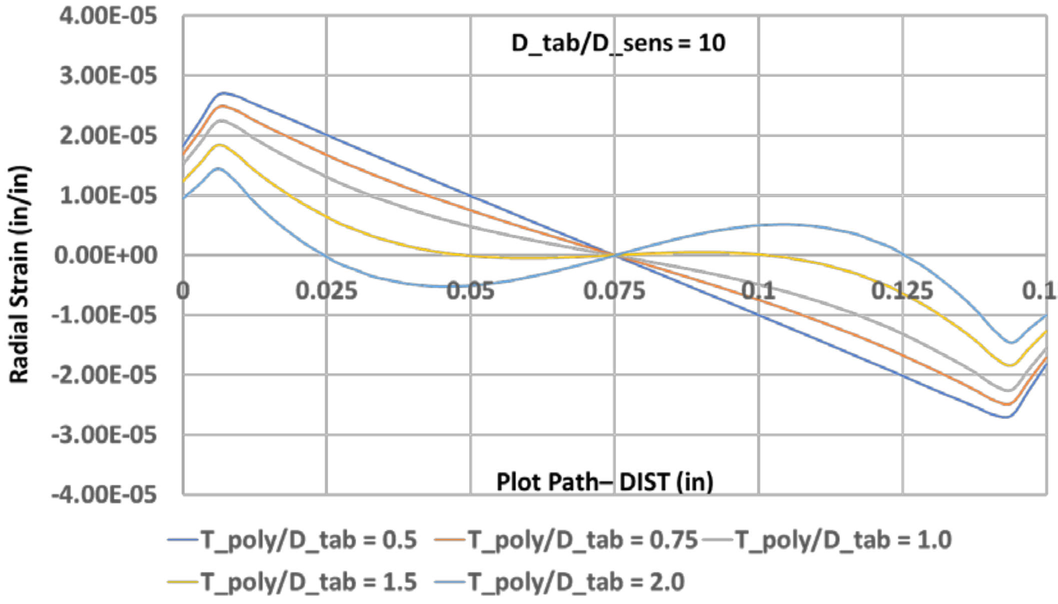

Figure 9: Radial Strain vs DIST for D_tab/D_sens = 10; T_poly/D_Tab varied

Figure 10 shows the models where the polymer thickness is equal to the endtab diameter, T_poly/D_tab = 1.0 and D_tab/D_sens ratios = 2, 3, 5, 7, and 10. The resulting Radial Strains vs Plot Path – DIST plots for each geometry are given in Figure 11. In this study, the ratio of polymer thickness to endtab diameter is held constant.

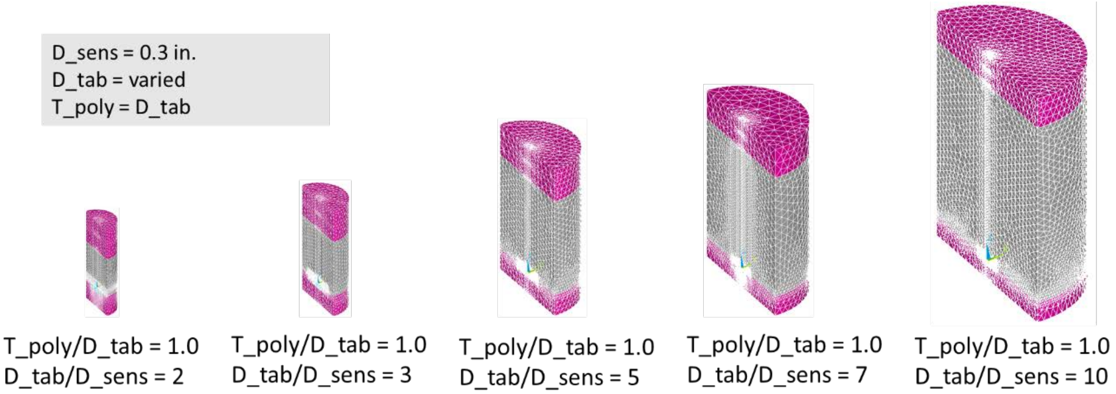

T_poly/D_tab = 1.0
D_tab/D_sens = 2

T_poly/D_tab = 1.0
D_tab/D_sens = 3

T_poly/D_tab = 1.0
D_tab/D_sens = 5

T_poly/D_tab = 1.0
D_tab/D_sens = 7

T_poly/D_tab = 1.0
D_tab/D_sens = 10

Figure 10: Parametric Models for T_poly/D_Tab = 1.0: D_tab/D_sens varied

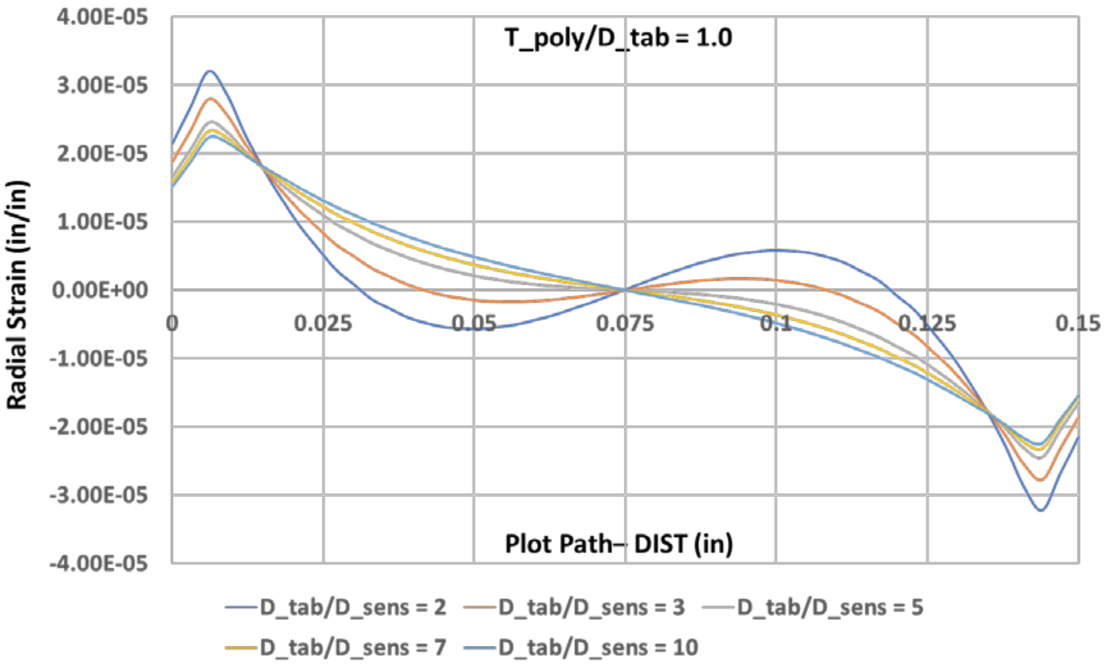

Figure 11: Radial Strain vs DIST for T_poly/D_Tab = 1.0; D_tab/D_sens = varied

Examining the parametric results for D_tab/D_sens = 3 and T_poly/D-tab = varied (Figure 7) reveals the diaphragm response is strongly influenced by the fixture geometry. Figure 12 shows an alternative view from the Figure 7 in terms of hoop and radial strains for the three configurations; D_tab/D_sens = 3 and T_poly/D-tab = 0.5, 1.0, and 2.0. For a height ratio of T_poly/D_tab, = 0.5, the diaphragm is highly constrained. For a height ratio of T_poly/D_tab = 2.0, the diaphragm is under constrained. A height ratio of T_poly/D_tab = 1.0 gave a good balance between the diaphragm being under constrained and being over constrained.

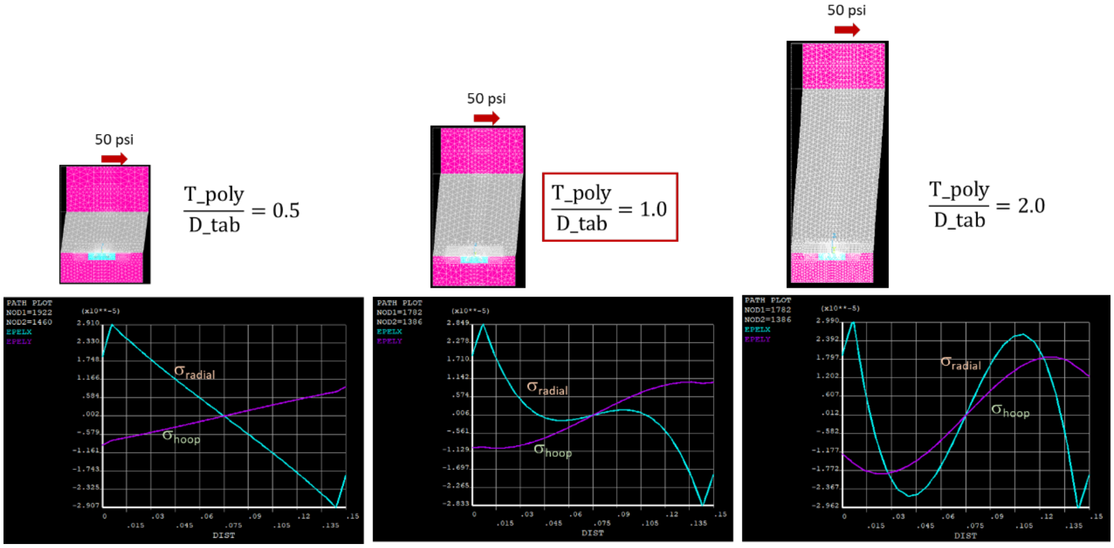

Figure 12: T_poly/D_tab = 1.0 geometry selected for Calibration Fixture (Does not over constrain nor under constrain diaphragm deformations)

A similar under or over constrained behavior can be seen in Figure 9 for D_tab/D_sens = 10 and T_poly/D-tab = varied. For a height ratio of T_poly/D_tab, = 0.5, the diaphragm is highly constrained. For a height ratio of T_poly/D_tab = 2.0, the diaphragm is under constrained. A height ratio of T_poly/D_tab = 1.0 gave a good balance between the diaphragm being under constrained and being over constrained.

Figure 11 shows the sensitivity of the D_tab/D_sens ratio. It is seen that the higher the D_tab/D_sens ratio, the lower the radial strain amplitude will be.

Based on these results, a calibration fixture geometry where D_tab/D_sens = 3 and T_poly/D-tab = 1 was selected because it will give a higher amplitude of strain with a reasonable degree of diaphragm motion while being a manageable fixture size for handling and preparation during NSST calibration testing.

4.2 Effect of Load Angle

The next parametric study examined the effect of load angle. The objective was to better understand the diaphragm strains under pure shear, pure normal and combined normal-shear loading conditions.

The calibration fixture geometry was set to the optimum values determined in Sec. 4.1, i.e. D_tab/D_sens = 3, and T_poly/D-tab = 1.0. The load angles, σ_angle = 0, 10, 15, 45, 75, 80, and 90 degrees were applied to the model (see Figure 13). Figure 14 plots the resulting radial strains along the same plot path described in Figure 5.

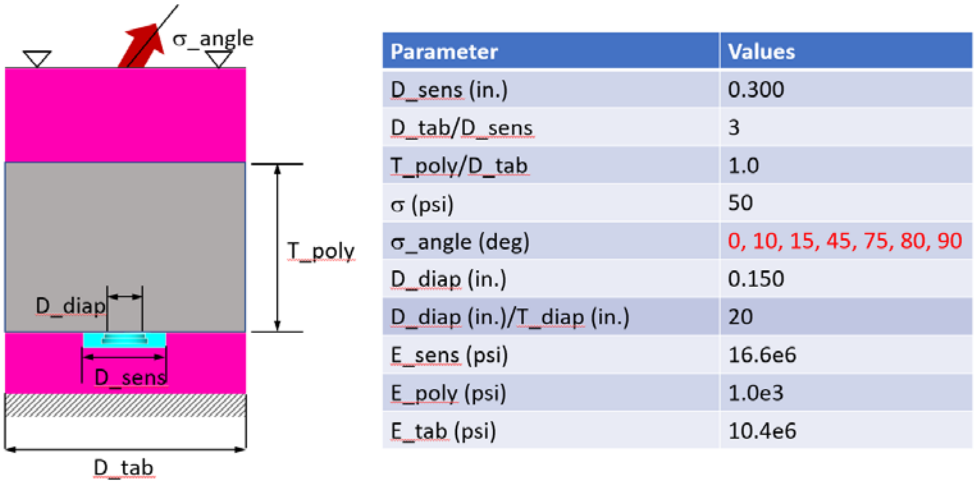

Parameter	Values
D_sens (in.)	0.300
D_tab/D_sens	3
T_poly/D_tab	1.0
σ (psi)	50
σ_angle (deg)	0, 10, 15, 45, 75, 80, 90
D_diap (in.)	0.150
D_diap (in.)/T_diap (in.)	20
E_sens (psi)	16.6e6
E_poly (psi)	1.0e3
E_tab (psi)	10.4e6

Figure 13: Calibration Fixture parameters used for Load Angle Studies.

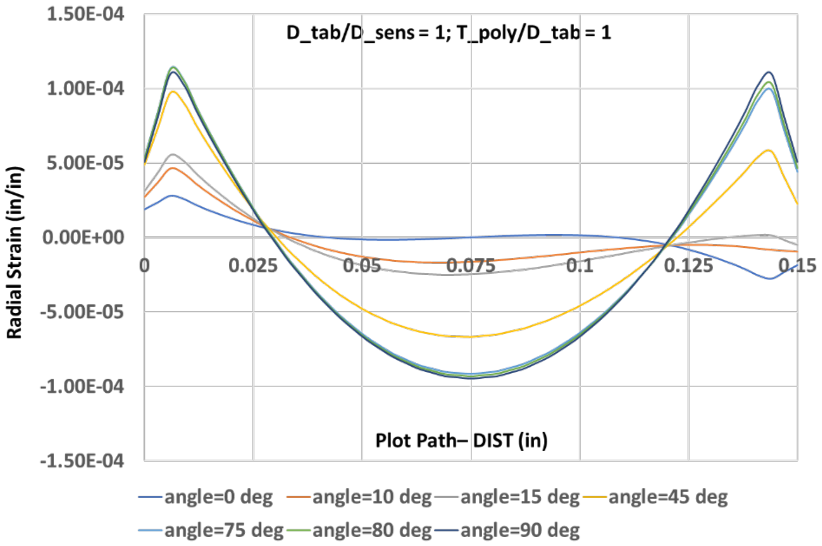

Figure 14: Radial Strain vs DIST Effects for σ_angle = varied

As seen in Figure 14, the peak radial strains occur at about 0.06 inches from the edges of the diaphragm and at the center when a normal stress component is present. A more detailed view of the load angle effect on the radial and hoop strains along the plot path-DIST is shown in Figure 15. Note that the Y-scales are not the same in the sub-plots. The sub-plots show that the diaphragm deforms in a characteristic manner depending on the loading angle. These characteristic deformation patterns can be used to measure the normal and shear bondline stresses independently and to deduce combinations of normal and shear stresses. Section 5.1 presents the method used to calculate the output shear and tensile strains (ε_shear and ε_tens) shown in the figure.

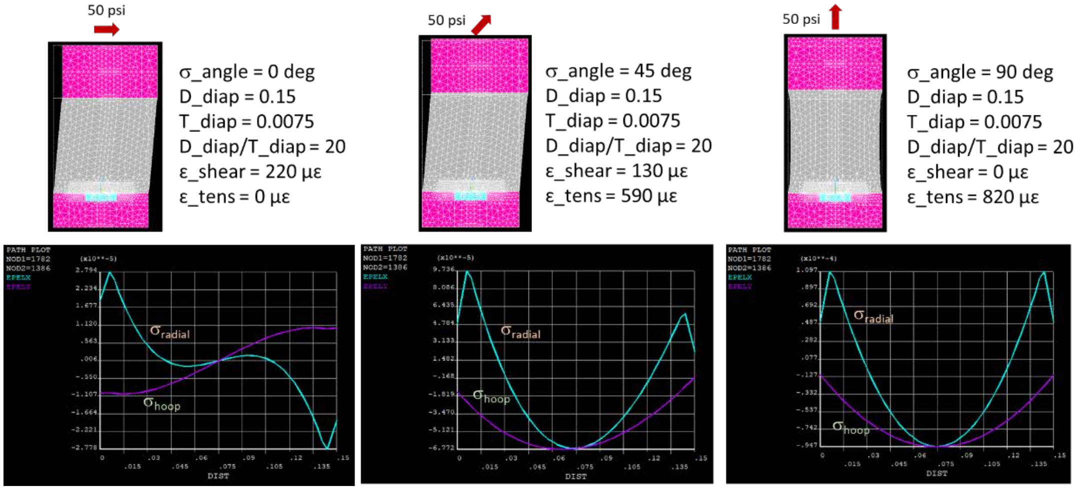

Figure 15: Calibration Fixture Parameters Used for Load Angle Studies.

4.3 Effect of Diaphragm Thickness

The current DBST sensor has a diaphragm thickness of 0.0075 in. This thickness has worked well for producing high strains under normal stresses up to 100 psi. However, as observed in Figure 15, the calculated tensile output signal, ε_tens = 590 με, is higher than the output signal for shear, ε_shear = 130 με, for a combined normal-shear loading case (σ_angle = 45 deg.).

It is desirable to increase the shear output if possible. Hence, an additional parametric analysis studied the effect of varying diaphragm thickness to maximize the shear output amplitude while minimizing the diaphragm-to-polymer interaction. It is important to keep the diaphragm stiff relative to the polymer modulus if consistent bondline stresses are to be measured.

Three diaphragm diameters, (D_diap) to diaphragm thicknesses (T_diap) were studied: D_diap/T_diap = 20, 30, and 35. Figure 19 shows the resulting normal stress across the top surface of the lower endtab for an equivalent 50 psi normal load at σ_angle = 90 deg. Ideally, the presence of the sensor diaphragm would have minimal influence on the normal stresses along the lower endtab. The circled regions in the sub-plots show that as the diaphragm gets thinner or D_diap/T_diap increases, the normal stress perturbation on top of the sensor gets larger. This perturbation is caused by the deformation of the diaphragm. It is desirable to keep the normal stress perturbation below 1 psi. A diaphragm thickness of a standard DBST would provide that result (D_diap/T_diap= 20, $\Delta\sigma$ = 0.9 psi). However, in order to increase the shear output for the NSST under combined loading conditions, the normal stress perturbation criterion must be relaxed. It was decided that a maximum normal stress perturbation less than 3 psi was acceptable. Therefore, a diaphragm thickness of D_diap/T_diap < 30 is required.

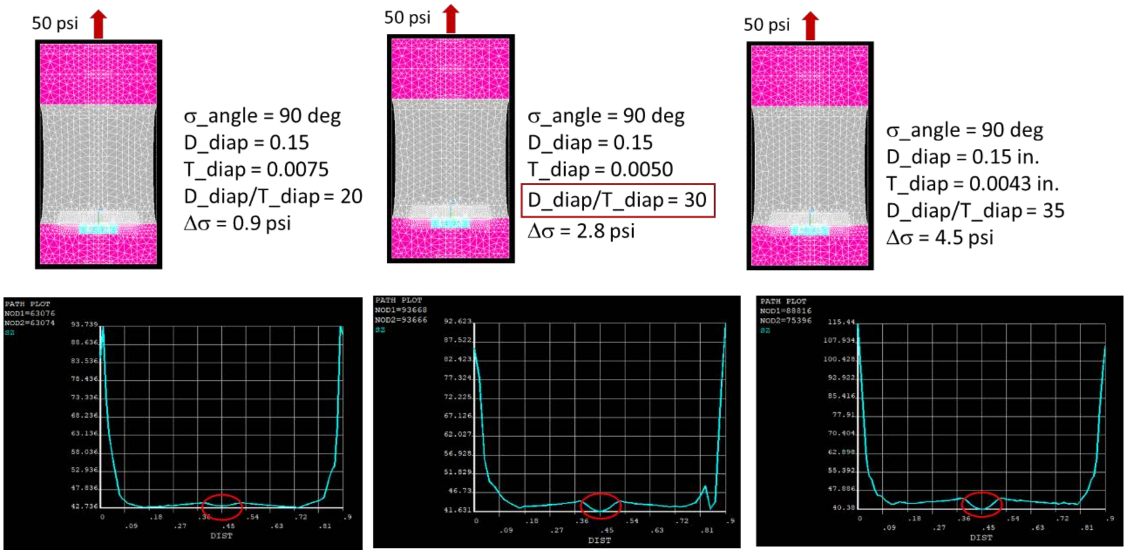

Figure 16: Effects of Diaphragm Thickness, D_diap/T_diap = 20, 30, and 35.

A diaphragm thickness of 0.0055 in. was selected. This thickness can be machined without warping problems. Figure 20 shows the calibration fixture geometry parameters and the corresponding calculated normal and shear outputs, ε_tens and ε_shear, at the loading angles of 0, 45 and 90 deg for this thickness. Comparing the shear and tensile outputs for a loading angle of 45 deg., Figure 15 (D_diap/T_diap = 20) and Figure 20 (D_diap/T_diap = 27) show that the strain outputs, ε_shear and ε_tens, are increased by 7% and 5%, respectively. Thus, a D_diap/T_diap = 27 gives a compromise between the need to increase the shear output and the need to minimize the stress perturbation over the top of the sensor.

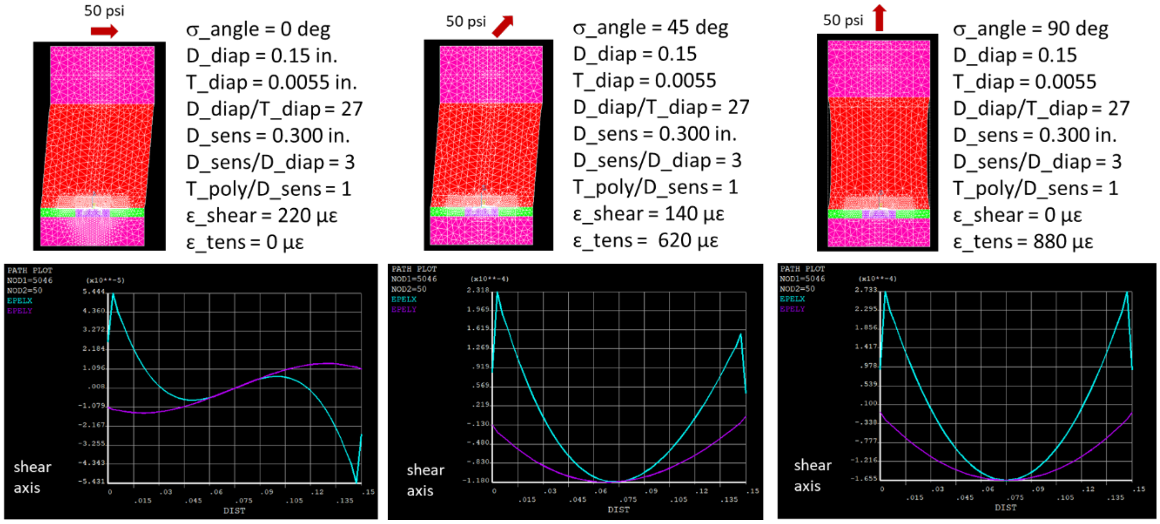

Figure 17: Final Design Parameters for the NSST Sensor and Calibration Fixture

4.4 Design Criteria for Calibration Fixture Displacement and Force

Calibration of the NSST will require a test apparatus or rig that can impose the same forces and displacements that are applied to the finite element model in this study. These displacements and applied forces (F/2) for an E_poly = 1000 psi are given in Figure 21.

Since a no-rotation constraint is imposed on the top endtab (see Sec. 3.1), this constraint suggests that an applied displacement-measure force approach would be more suitable for a calibration rig concept than an applied force-measure displacement concept.

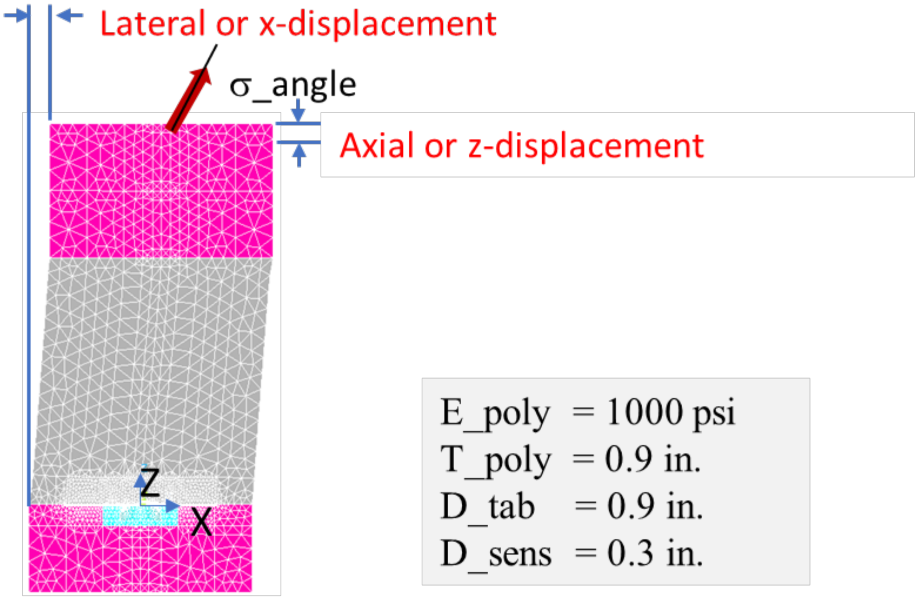

Angle	X-displacement / Force/2	Z-displacement / Force/2
0 deg (shear)	0.213 in. / 15.9 lb.	- 0.11e-4 in / 0 lb.
45 deg ……	0.151 in. / 11.24 lb.	0.029 in. / 11.24 lb.
90 deg (tension)	0 in. / 0 lb.	0.041 in. / 15.9 lb.

Figure 18: Design Displacements and Forces (F/2) for NSST Calibration Rig

5. GENERAL GAGE PLACEMENT AND DATA ANALYSIS

5.1 Strain to Electrical Signal Transformation

A Wheatstone bridge is used to transform the strain gage's change in resistance, as a function of a mechanical load, into an electrical output. The theory of Wheatstone bridge operation is well documented in the open literature [11].

Assuming all strain gages have the same nominal resistance and the change in resistance is small with respect to the nominal resistance, the general equation for the Wheatstone bridge is

$$\frac{e_0}{E_{exc}} = \frac{1}{4}\left(\frac{\Delta R_1}{R} - \frac{\Delta R_2}{R} + \frac{\Delta R_3}{R} - \frac{\Delta R_4}{R}\right) \qquad (1)$$

where

e_0 is the bridge output,

E_{exc} is the bridge excitation voltage,

R is the nominal strain gage resistance,

ΔR_n is change in resistance of strain gage n.

The convention used for the numbering of the strain gages is shown in Figure 19.

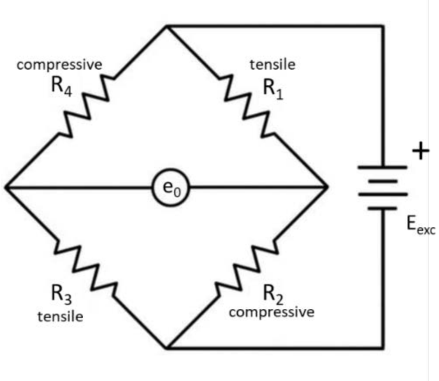

Figure 19: Schematic of a Wheatstone Bridge

It can be seen from Figure 19 and equation 1 that maximum bridge output, e_0/E_{exc} , is obtained if strain gages R1 and R3 are located in areas of tension and strain gages R2 and R4 are located in areas of compression giving

$$\frac{e_0}{E_{exc}} = \left(\frac{\Delta R}{R}\right) \qquad (2)$$

if all changes in gage resistance, ΔR, are the same.

5.2 Finite Element Analysis Results for Varying Load Angle

A finite element study of the NSST diaphragm for a loading condition that varies from pure shear to pure tension was repeated for the selected calibration geometry $D_{endtab}/D_{sensor} = 3$ and $T_{poly}/D_{endtab} = 1$. The predicted diaphragm strain profiles are used to select the gage locations and to implement the Wheatstone bridges that will allow extraction of the normal stress, shear stress and loading angle from the Wheatstone bridge output voltages.

Table 3 lists the model's mechanical properties and geometry while Figure 20 shows the sign convention used for the load angle and the load direction.

Table 3. Calibration Fixture Geometry and Mechanical Properties

Component	Property	Value
Endtab	Modulus E (psi) Poisson ratio D_{endtab}/D_{sensor}	10.4×10^6 0.32 3
Polymer	Modulus E (psi) Poisson ratio T_{poly}/D_{endtab}	1000 0.495 1
Sensor	Modulus E (psi) Poisson ratio D_{sensor} (in.) $D_{diaphragm}$ (in.) $T_{diaphragm}$ (in.)	16.6×10^6 0.34 0.300 0.150 0.0075
Load	Pressure (psi) Load Angle (deg)	50 0, 10, 15, 45, 75, 80, 90
Load angle is defined relative to the diaphragm surface and increases positively to the surface normal.		

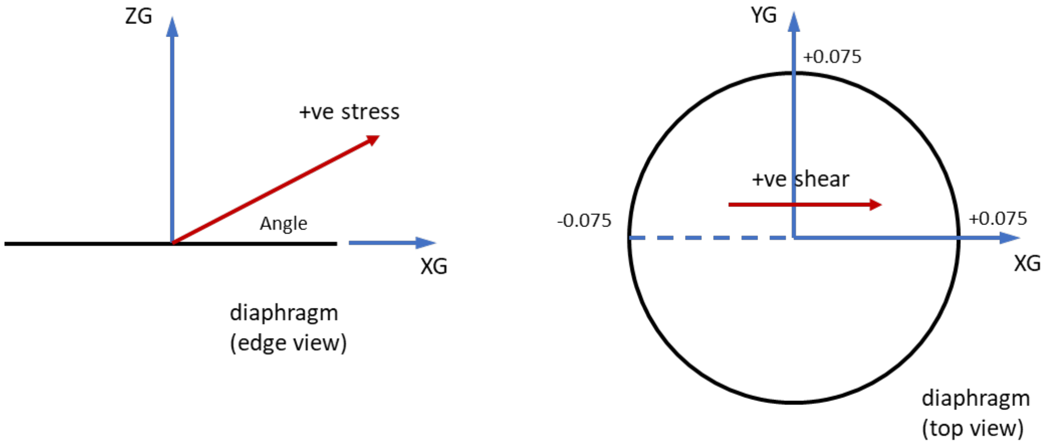

Figure 20: Sign Convention for Applied Load on Diaphragm

The overall fixture deformation and the sensor diaphragm radial (EPELX) and circumferential (EPELY) strain results are provided in Figures 21 to 27 for the different load angles. The values represent the strains found on the bottom-side of the diaphragm. Several observations can be made:

a) At a load angle of 0 deg., i.e. pure shear (Figure 21), the radial and circumferential diaphragm strains have an anti-symmetric profile across the diaphragm as expected.

b) At a load angle of 90 deg., i.e. pure tension (Figure 27), the radial and circumferential diaphragm strains have a symmetric profile across the diaphragm as expected.

c) For 0 < load angle < 15 deg. (Figure 22 and Figure 23), the radial strains at 0.075 in. < X-coord < 0.150 in. drop relative to the radial strains at 0.000 < X-coord < 0.075 in. while the opposite is true for the circumferential strains.

d) At a load angle of 45 deg. (Figure 24), the radial strains at 0.075 in. < X-coord < 0.150 in. rise relative to the radial strains at 0.000 < X-coord < 0.075 in. The opposite is true for the circumferential strains.

e) For 75 < load angle < 90 deg. (Figure 25 and Figure 26), the radial and circumferential strain profiles are approaching a symmetric shape.

It was not necessary to calculate the diaphragm strains at other load magnitudes because the strains experienced by the diaphragm are small enough that the diaphragm behavior remains linear elastic, i.e. the sensor material does not enter a nonlinear behavior regime. Thus, the linear elastic analysis guarantees a diaphragm strain that is proportional to applied load.

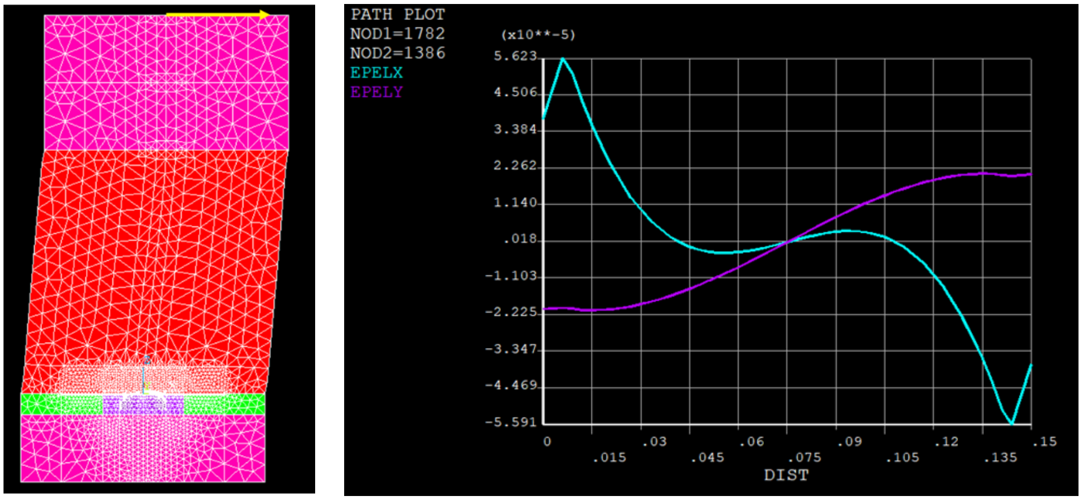

Figure 21: Deformation and Diaphragm Strains for Load Applied at 0 deg.

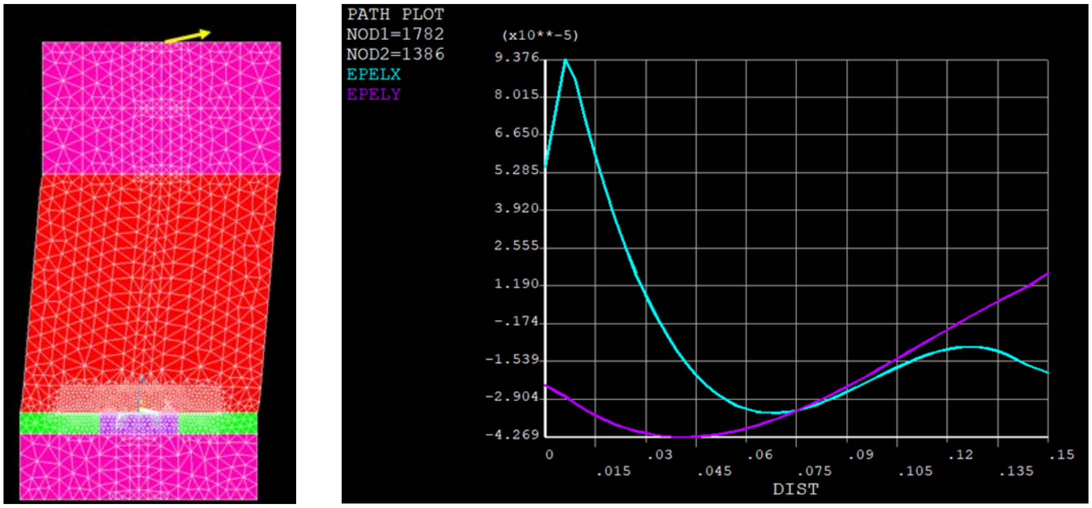

Figure 22: Deformation and Diaphragm Strains for Load Applied at 10 deg.

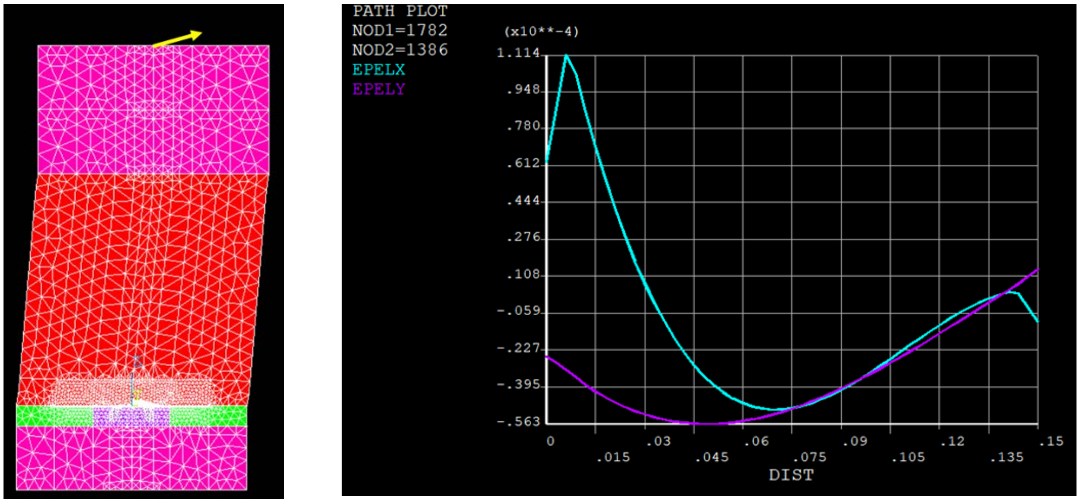

Figure 23: Deformation and Diaphragm Strains for Load Applied at 15 deg.

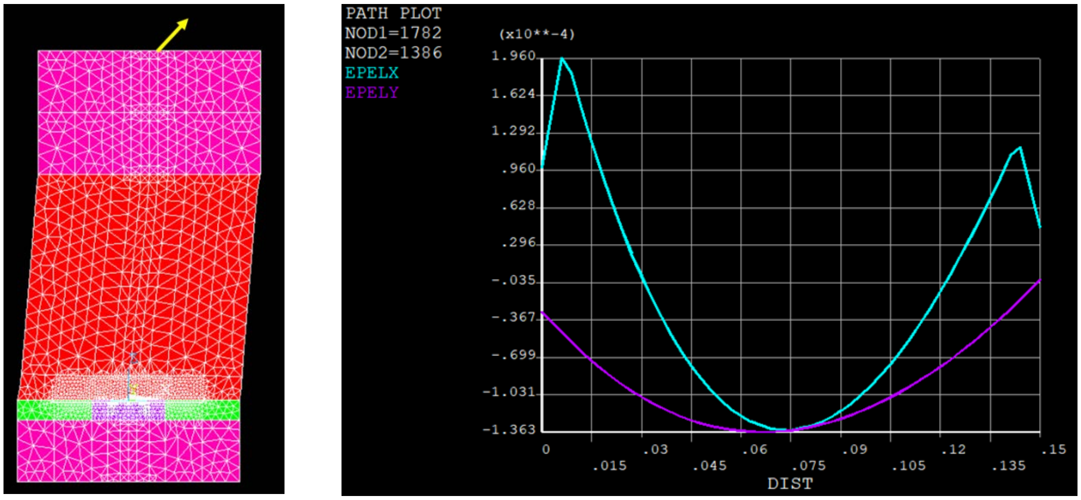

Figure 24: Deformation and Diaphragm Strains for Load Applied at 45 deg.

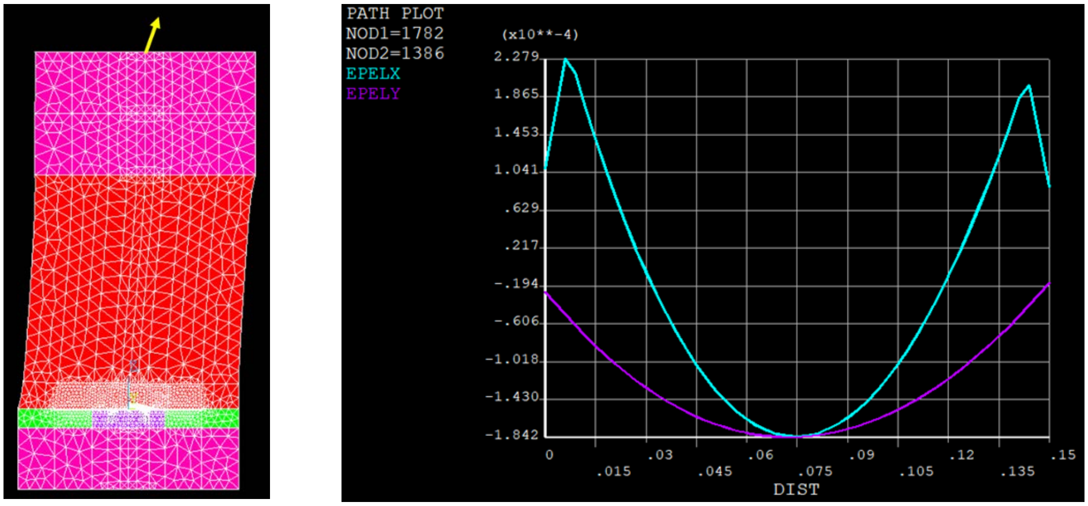

Figure 25: Deformation and Diaphragm Strains for Load Applied at 75 deg.

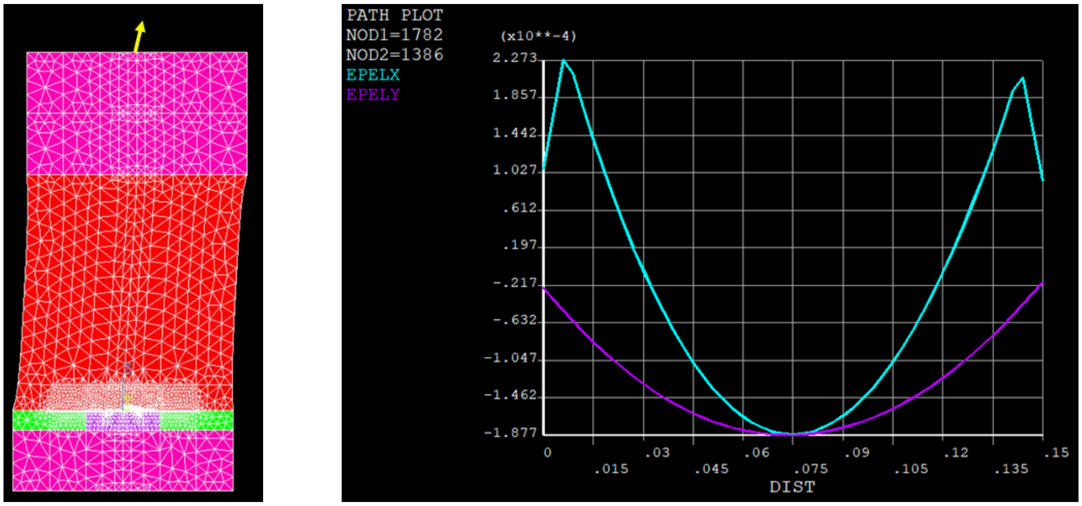

Figure 26: Deformation and Diaphragm Strains for Load Applied at 80 deg.

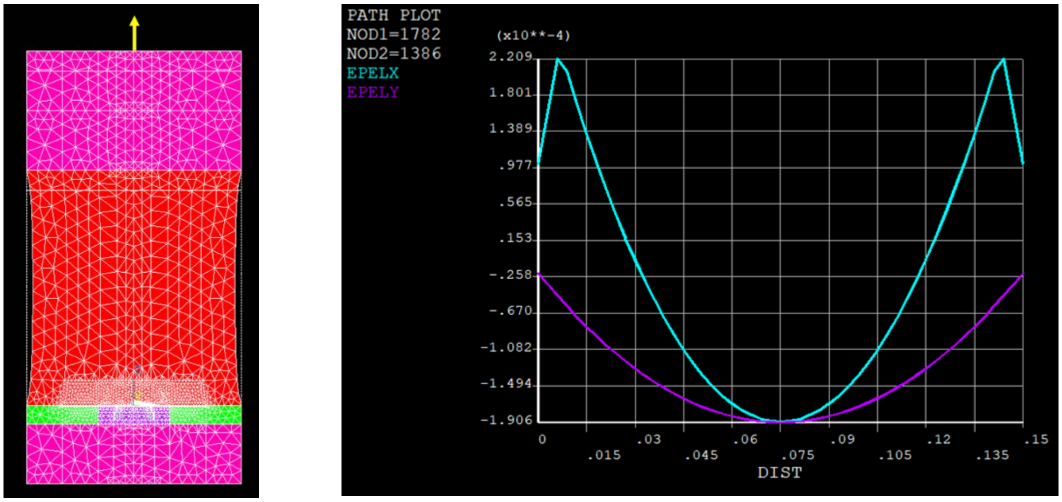

Figure 27: Deformation and Diaphragm Strains for Load Applied at 90 deg.

5.3 Gage Placement

The strain profiles in Figures 21 to 27 show that a diaphragm instrumented with a set of strain gages that are connected into a Wheatstone bridge could be used to calculate the load magnitude and direction. Either the radial or circumferential profiles could be used. However, it is more advantageous to use radial strain because it is the larger strain quantity. As mentioned in Section 5.1, maximum bridge output occurs when there are two strain gages that experience tension and two strain gages that experience compression on the sensor diaphragm.

Examining the pure positive shear case (Figure 21), at Dist = 0.015 in. on the diaphragm diametrical axis, the radial strain on the bottom-side of the diaphragm is roughly +33.8 microstrain. On the other end of the diaphragm at Dist = 0.135 in., the radial strain is -33.5 microstrain.

Visual examination of the radial strain results in Figures 22 to 26 shows that two gages placed at Dist = 0.015 in. and two at Dist = 0.135 in. could provide a unique bridge output for an applied shear stress.

Changing to the pure tensile load case (Figure 27), at Dist = 0.015 in. and Dist = 0.135 in., the radial strain on the bottom-side of the diaphragm is symmetric and roughly +133 microstrain. At Dist = 0.0 in., the radial strain is roughly -191 microstrain.

These results led to the following conclusions for gage placement:

1. For the shear bridge, two gages placed at Dist = 0.015 in. and two at Dist = 0.135 in. along the diaphragm’s diametrical axis would produce a unique bridge output that is

proportional to an applied shear stress. These locations would provide space to allow a strain gage to be oriented in a radial orientation without interfering with the sensor rim.

2. For the normal bridge, one gage placed at Dist = 0.015 in. and Dist = 0.135 in. and two side-by-side gages at Dist = 0.0 in. would provide a unique bridge output for a normal stress component.

Since the normal stress is load direction independent, it is not necessary to orient a normal stress bridge along any particular axis of a loaded structure. The orientation axis of the shear stress bridge, however, needs to be aligned along the same axis as the expected shear stress in order maximize its output.

Figure 28 shows schematically the positions of the eight strain gages on the backside of the NSST sensor diaphragm.

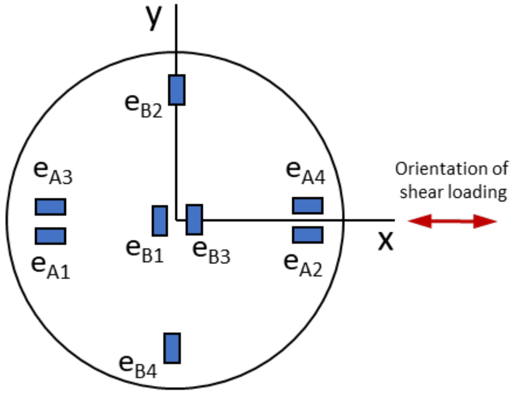

Figure 28: Strain Gage Placement on Sensor Diaphragm for Measuring Normal and Shear Loading Conditions.

Table 4. Gage Placement on NSST Diaphragm

Bridge	**Bridge Element**	**Gage**	**X-coord (in.)**	**Y-coord (in.)**
Shear	R1	e_{A1}	-0.060	-0.005
	R2	e_{A2}	+0.060	-0.005
	R3	e_{A3}	-0.060	+0.005
	R4	e_{A4}	+0.060	-0.005
Normal	R1	e_{B1}	-0.005	0.0
	R2	e_{B2}	0.0	+0.060
	R3	e_{B3}	+0.005	0.0
	R4	e_{B4}	0.0	-0.060

5.4 NSST Data Reduction

The NSST data reduction is a straightforward procedure when the shear bridge is aligned with a major axis of shear acting in a structure. For a solid rocket motor, the major axis of shear coincides with the longitudinal axis of the motor. The data reduction is more complicated if the shear stresses are acting at an angle not aligned with a major axis of shear. In this section, the analysis for a shear bridge purposely aligned with the longitudinal axis of the rocket motor, i.e. major axis of shear, is presented. Annex A details the gage placement and data reduction of a sensor that does not have its shear bridge aligned with a major axis of shear.

5.4.1 Finite Element Results

To demonstrate the data reduction method, the finite element results from Section 5.2 at the gage locations specified in Table 4 and equation 1 are used to generate sample bridge data. Thus, the normal and shear bridge outputs for a load angle varying from 0 to 90 deg are shown in Figure 29.

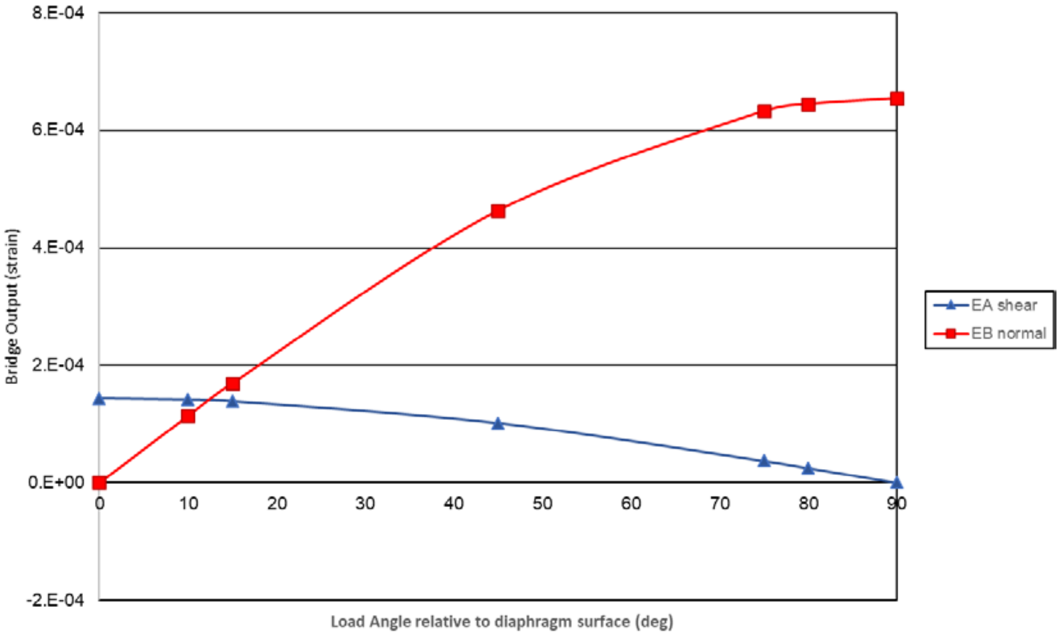

Figure 29: Predicted Shear and Normal Bridge Outputs. Load Angles Vary from 0 deg. to 90 deg.

5.4.2 NSST Calibration

The NSST requires two calibration factors. One for pure shear and one for pure tension or compression. The calibration factors are defined by

$$K_{shear} = \frac{F_{applied}}{A_{endtab}E_{A0}} \tag{5}$$

$$K_{norm} = \frac{F_{applied}}{A_{endtab}E_{B0}} \tag{6}$$

where

$F_{applied}$ is the known applied load,

A_{endtab} is the known surface area over which the load is applied,

E_{A0} is the measured electrical shear bridge output,

E_{B0} is the measured electrical normal bridge output,

K_{shear} is the calibration factor for the shear bridge output,

K_{norm} is the calibration factor for the normal bridge output.]

5.4.3 Recuperation of Normal and Shear Stresses and Loading Angle

The normal and shear stresses in engineering units are easily calculated using the calibration factors from equations 5 and 6. Since the shear bridge is aligned with major axis of shear, the loading angle, ϕ, is a function of the normal stress to shear stress ratio.

$$\tau = K_{sscf}K_{shear}E_A \tag{7}$$

$$\sigma = K_{nscf}K_{norm}E_B \tag{8}$$

$$\phi = \tan^{-1}\frac{\sigma}{\tau} \tag{9}$$

where

E_A is the measured shear bridge output,

E_B is the measured normal bridge output,

K_{sscf} is the stress concentration factor for the shear bridge output,

K_{nscf} is the stress concentration factor for the normal bridge output.

K_{shear} is the calibration factor for the shear bridge output,

K_{norm} is the calibration factor for the normal bridge output.

τ is the calculated shear stress,

σ is the calculated normal stress,

ϕ is the calculated loading angle.

The stress concentration factors, K_{sscf} and K_{nscf} are included here to account for any stress concentrations due to the geometric discontinuity in the solid propellant that is introduced by the installation of the NSST. The stress concentration factors are calculated by a finite element model of the NSST as it is actually installed in a rocket motor.

6. CORRESPONDENCE BETWEEN NSST CALIBRATION BONDLINE STRESSES AND STRUCTURAL TEST VEHICLE BONDLINE STRESSES

The target application for the NSST sensor is to monitor the normal and shear stresses at the interface of two bonded components. In a structural test vehicle, the interface of interest occurs at a case-polymer bondline near a bond termination.

Figure 30 shows an axisymmetric model of a 10-inch diameter structural test vehicle where a cylindrical metallic case is filled with a polymer having a web fraction of 0.8 (i.e. centerbore diameter of 2-in.). The accompanying graph is a plot of the radial or normal stress and the shear stress along the bondline when the structural test vehicle is under a cooling thermal load.

The graph shows that the shear is maximum near the bond termination (Bondline distance = 0). The red circled region highlights the fact that near the bond termination, the radial or normal stress is nearly equal to the shear stress. This observation suggests that if a load is applied to the NSST calibration fixture at an angle of 45 deg., it would simulate the same stress state seen in a structural test vehicle.

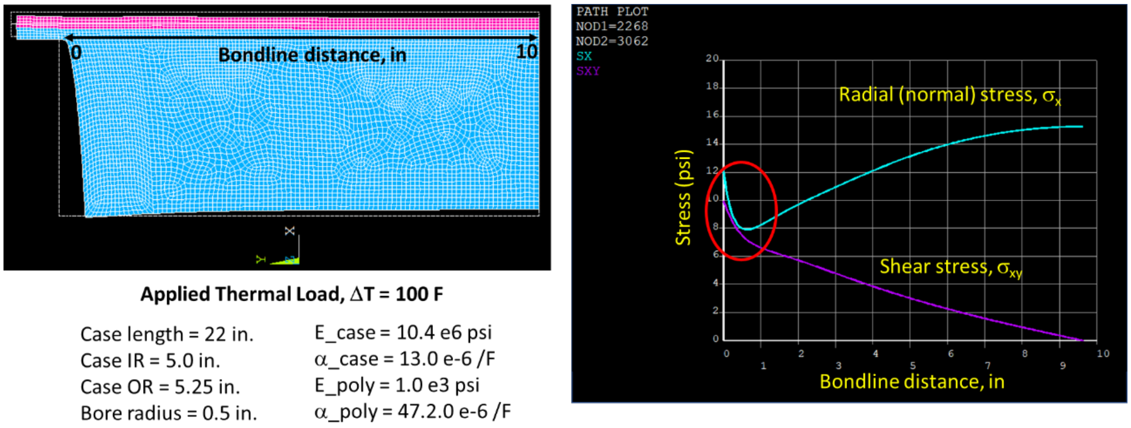

Figure 30: Generic Structural Test Vehicle Bondline Stresses

To validate this assumption an analysis was performed with a NSST modeled in a structural test vehicle. The diaphragm response of a NSST in a calibration fixture with an applied load angle of 45 degrees was then compared to the diaphragm response of the NSST mounted in the structural test vehicle.

Figure 31 shows the model of the NSST mounted in the structural test vehicle. The NSST is mounted on a shim placing the center of the sensor 0.375 in. from the edge of the bond termination. The accompanying graph is a plot of the radial (normal) and shear stresses over the NSST. The red box highlights the region over the NSST diaphragm.

The graph confirms that the shear and normal stresses are approximately equal in magnitude over the diaphragm.

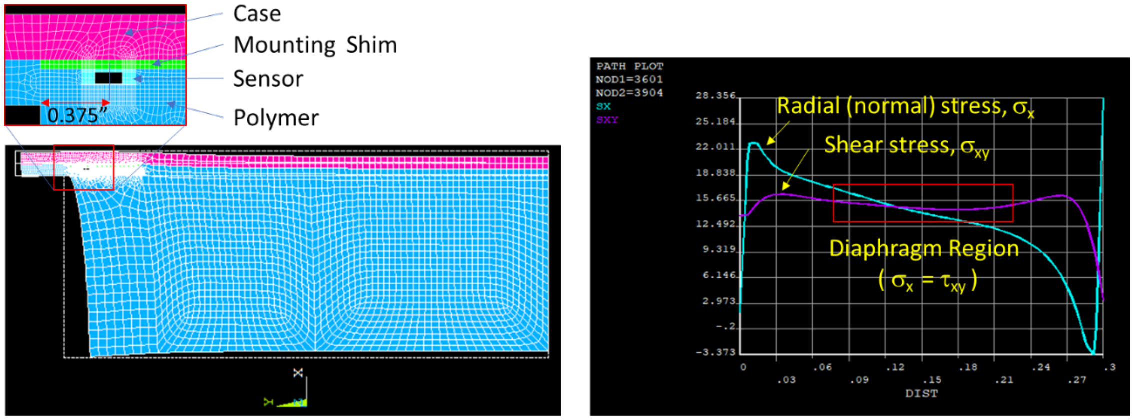

Applied Thermal Load, ΔT = 100 F

Figure 31: Structural Test Vehicle Modeled with a Mounted NSST

Figure 32 show graphs comparing the diaphragm strains of a NSST mounted in the structural test article under a thermal stress and a NSST mounted in a calibration fixture with a load applied at 45 deg. The shapes of the radial strain curves are comparable. Hence, it can be said that a load applied at an angle of 45 deg. on a calibration fixture will simulate the state of stress at a bond termination in a structural test vehicle.

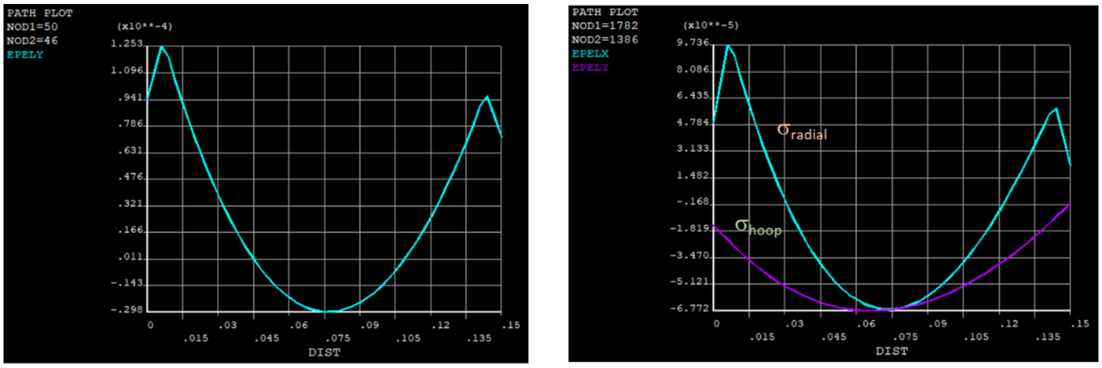

a) Sensor Diaphragm Radial Strain for Structural Test Article under Thermal Load

b) Sensor Diaphragm Radial Strain for Calibration Fixture, σ_angle =45

Figure 32: Comparison of Diaphragm Radial Strains for a NSST in a Structural Test Vehicle and in a Calibration Fixture with a σ_angle =45 deg.

7. SUMMARY

The objective of this study was to numerically determine the potential performance of a diaphragm-based normal shear stress and temperature (NSST) sensor design. The results of the parametric study were presented and discussed. The principal parameters controlling the deformation of the diaphragm under combined stress loading were found to be: 1) the stiffness of the polymer, 2) the thickness of the polymer on top of the sensor to the loading surface diameter ratio, 3) the loading surface diameter to the sensor diameter ratio, 4) the diaphragm diameter of the sensor, and 5) the diaphragm thickness.

The optimal geometry of the fixture needed to calibrate the NSST was determined to be:
a) thickness of the polymer on top of the sensor to the loading surface diameter ratio = 1,
b) loading surface diameter to the sensor diameter ratio = 3,
c) sensor diameter = 0.30 in.
d) diaphragm diameter of the sensor = 0.15 in.
e) diaphragm thickness = 0.0055 in.
It was shown that the NSST diaphragm had adequate stiffness to minimize the diaphragm-to-polymer interaction.

A comparison between a NSST mounted near the bond termination in a structural test vehicle under a thermal load and a NSST mounted in a calibration fixture with a load applied at 45 deg. showed the diaphragm strain responses were similar. This result confirmed that the calibration fixture geometry imposes a stress field that is similar to the one found in a thermally cooled structural test vehicle.

In future work, a calibration rig that applies normal and shear loads individually or in combination will be designed and built. Particular attention will be paid to the mechanical design features that will reproduce the stress fields and displacement constraints modeled in the finite element study.

8. REFERENCES

[1] Anderson, J.M. et al., “Techniques for Assessing Case Liner-Bond Integrity in Solid Propellant Rocket Motors”, AFRPL-TR-73-75, Sep. 1973.

[2] Francis, EC, Chelner, H, (1977), “Design of high stability stress transducer”, 23rd International Instrumentation Symposium, Instrument Society of America.

[3] Francis, EC, Thompson, RE, (1982), “Solid propellant stress transducer design and stability data”, 28th International Instrumentation Symposium, Instrument Society of America.

[4] Micron Instruments, (2014), “DBST Sensor Assembly Drawings”.

[5] Mueller, RA, Chelner, H, “DBST safety via inherent semiconductor strain gage fusion”, JANNAF 2015 Meeting, Salt Lake City, UT, Dec. 2015.

[6] Chelner, H, Mueller, RA, “Worst-case over-voltage protocol results for DBST sensors embedded in solid rocket motors”, JANNAF 2016 Meeting, New Port News, VA, May 2016.

[7] Francis, EC, (1988), “Shear stress transducer review meeting”, contract sponsored by U.S. Air Force Astronautics Laboratory, Contract No. FO4611-87-C-0062.

[8] Francis, EC, Thompson, RE, Heerema, SW, (1990), “Shear stress transducer concepts”, 1990 JANNAF Meeting.

[9] https://www.ansys.com/products/structures/ansys-mechanical-enterprise, accessed 11 July 2019.

[10] Little, RR, Tucker, D, Wong, FC, White, A, “Mechanical Aging of Solid Rocket Motors”, TTCP WPN Technical Panel 4 Energetic Materials and Propulsion KTA 4-29 Final Report Vol. 1, April 2006.

[11] Hoffman, K., “Applying the Wheatstone Bridge Circuit”, http://eln.teilam.gr/sites/default/files/Wheatstone%20bridge.pdf, accessed 21 Sep. 2017.

This page intentionally left blank.

ANNEX A – GENERAL PURPOSE NSST

Section 5 described the gage placement and data analysis for a NSST where its shear bridge is purposely aligned with a known major axis of shear. There may be other applications where the shear vector changes direction relative to the shear bridge depending on the loading condition. This Annex details the gage placement and data analysis for a NSST that can measure simultaneously the magnitude and orientation of shear stress and the magnitude and direction of normal stress.

A.1 Loading Angle Definition

Figure A1 shows definitions used to define the normal stress loading angle, ϕ, and the stress stress loading angle, θ, relative to a global cartesian coordinate system.

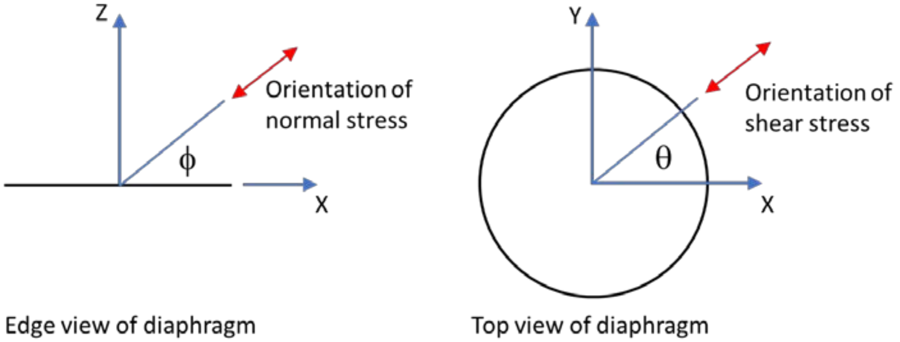

Figure A1. Definition of Loading Angles.

A.2 Finite Element Study

A finite element study similar to the one described in Section 5.2 was carried out. In this case, the shear stress loading angle, θ, was varied over a range of 0 to 90 deg. The same material properties and sensor dimensions as Table 5 were used. For the sake of brevity, only the radial strain results for the parametric study are provided. As shown in Figure A2, a shear stress of -50 psi was applied to the diaphragm.

There is an artifact of the finite element solution at X = 0. An attempt was made to find the cause of this artifact. However, the search was unsuccessful due to lack of time. The results can still be used for data analysis development because the strain trends are reasonable for the various load angles.

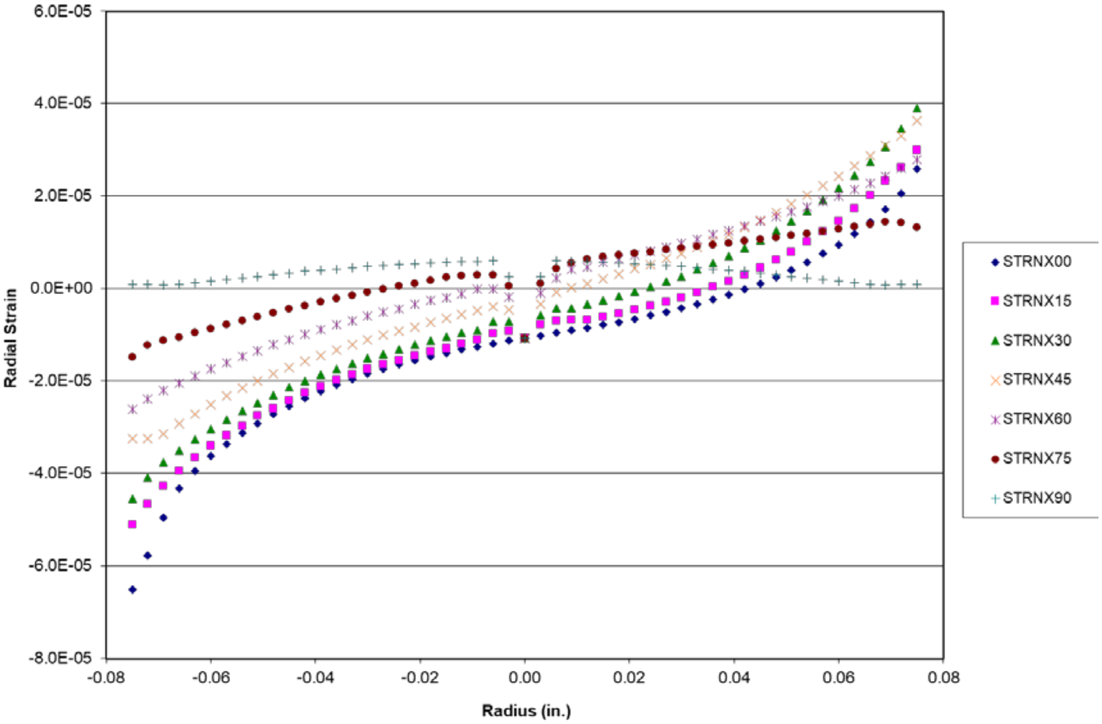

Figure A2. Radial strain variation across diaphragm with shear stress angle for a negative applied shear stress.

A.3 Gage Placement

The logic used for gage placement is Section 5.3 is used here as well. In this case, it is necessary to have two shear stress bridges in order to deduce the shear stress orientation, θ, from the bridge measurements. Again, since the normal stress is independent of loading angle, ϕ or θ, the normal bridge axis is located at $\theta = 135$ deg. for convenience (see Figure A3).

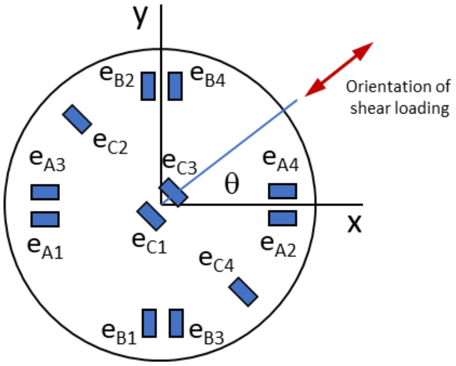

Figure A3. Strain Gage Placement on Sensor Diaphragm for Measuring Normal and Shear Loading Conditions.

A.4 Data Reduction Development

The relationship between strain resistance change and Wheatstone bridge output (equation 1) is repeated here in equation A1.

$$\frac{E_0}{E_{exc}} = \frac{1}{4}\left(\frac{\Delta R_1}{R} - \frac{\Delta R_2}{R} + \frac{\Delta R_3}{R} - \frac{\Delta R_4}{R}\right) \tag{A1}$$

where

E_0 is the bridge output,

E_{exc} is the bridge excitation voltage,

R is the nominal strain gage resistance,

ΔR_n is change in resistance of strain gage n.

The voltage outputs of the three bridges are designated as

E_{0A} is the bridge output for shear bridge A

E_{0B} is the bridge output for shear bridge B

E_{0C} is the bridge output for normal bridge C

It is advantageous to use the derived quantities $E_{0A}+E_{0B}$ and $E_{0A}-E_{0B}$. Plotting the quantities $E_{0A}+E_{0B}$, $E_{0A}-E_{0B}$ and E_{0C} as a function of load angle, θ, results in the graph shown in Figure A4.

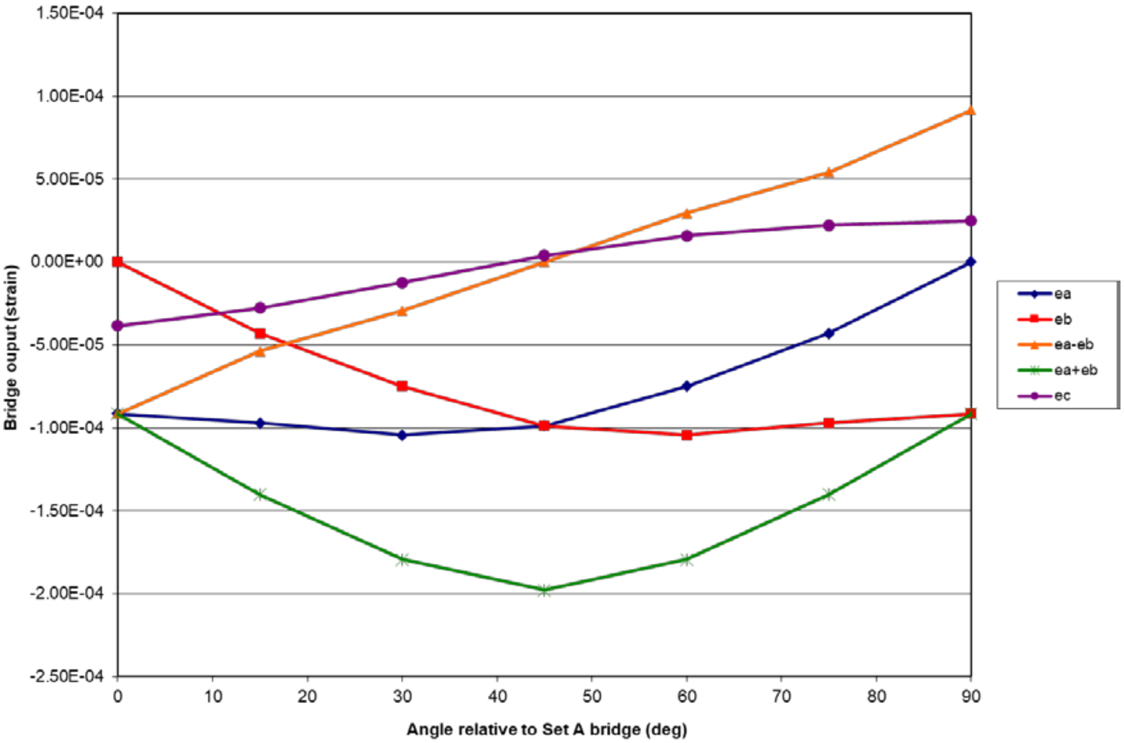

Figure A4. Bridge Outputs and Derived Bridge Outputs as Function of Shear Loading Angle.

Inspection of Figure A4 reveals that E_{0A}-E_{0B} has a linear relationship with loading angle. For $E_{0A}+E_{0B}$, it has a second-order polynomial relationship with loading angle. These relationships can be normalized and expressed as,

$$\frac{E_{0A} - E_{0B}}{E_{0sref}} = K_m\theta + K_b \qquad \text{(A2)}$$

$$\frac{E_{0A} + E_{0B}}{E_{0sref}} = K_1\theta^2 + K_2\theta + K_3 \qquad \text{(A3)}$$

where

E_{0A} is the shear bridge A output,

E_{0B} is the shear bridge B output,

E_{0sref} is the measured shear bridge output for a known shear stress acting along the axis of shear bridge A or B (refer to Figure A3).

K_n are the fitting coefficients found using a numerical curve-fitting method.

The measurement of the shear bridge at a reference condition requires a calibration device that allows a known force to be applied in pure shear to the NSST along the axis of the shear bridge. The bridge output, E_{0ref}, is measured when the force is applied. The calibration factor, K_{shear}, is also calculated at the same time using

$$K_{shear} = \frac{\tau_{appl}}{K_{sscf} E_{0sref}} \qquad \text{(A4)}$$

where

τ_{appl} is the known applied pure shear stress based on a known force, F_{appl}, acting over a known calibration fixture area, A_{endtab},

K_{sscf} is the stress concentration factor due a geometric discontinuity in the calibration configuration if one exists,

E_{0sref} is the measured electrical shear bridge output,

K_{shear} is the calibration factor for the shear bridge output.

The value of K_{sscf} is calculated by finite element modeling of the calibration device and the installed NSST.

The calculation of the normal bridge calibration factor, K_{norm}, follows a procedure like the one used for the shear bridge.

$$K_{norm} = \frac{\sigma_{appl}}{K_{nscf} E_{0nref}} \qquad \text{(A5)}$$

where

σ_{appl} is the known applied pure normal stress based on a known force, F_{appl}, acting over a known calibration fixture area, A_{endtab},

K_{nscf} is the stress concentration factor due a geometric discontinuity in the calibration configuration if one exists,

E_{0nref} is the measured electrical normal bridge output,

K_{norm} is the calibration factor for the normal bridge output.

The value of K_{nscf} is calculated by finite element modeling of the calibration device and the installed NSST.

A.5 Recuperation of Normal and Shear Stresses and Loading Angle

Once the fitting coefficients, K_n, and calibration factor for the shear bridge, K_{shear}, are found, these values can be used with equations A2 and A3 to recuperate the acting shear stress and its angular orientation with respect to a selected shear bridge in a structure.

Equations A2 and A3 can be re-written by substituting in a re-arranged form of equation A4. The resulting equations are

$$\frac{C_1}{\beta} = K_m\theta + K_b \tag{A6}$$

$$\frac{C_2}{\beta} = K_1\theta^2 + K_2\theta + K_3 \tag{A7}$$

where

$$C_1 = E_{0A} - E_{0B} \tag{A8}$$

$$C_2 = E_{0A} + E_{0B} \tag{A9}$$

$$\beta = \frac{\tau_{meas}}{K_{sscf}K_{shear}} \tag{A10}$$

Equations A6 and A7 are two equations with two unknowns, τ_{meas} and θ. The bridge outputs, E_{0A} and E_{0B}, are measured quantities. Re-arranging equation A6 and substituting it into equation A7 with appropriate manipulation gives

$$0 = C_3\beta^2 + C_4\beta + C_5 \tag{A11}$$

where

$$C_3 = \frac{K_1K_b^2}{K_m^2} - \frac{K_bK_2}{K_m} + K_3 \tag{A12}$$

$$C_4 = \frac{K_2C_1}{K_m} - \frac{2K_1C_1K_b}{K_m^2} - C_2 \tag{A13}$$

$$C_5 = \frac{K_1C_1^2}{K_m^2} \tag{A14}$$

Solving equation A11 for β and substituting in equation A10 gives the solution (equation A15) for the measured shear stress, τ_{meas}, given the measured shear bridge outputs E_{0A} and E_{0B}.

$$\tau_{meas} = K_{sscf}K_{shear}\left(\frac{-C_4 - \sqrt{C_4^2 - 4C_3C_5}}{2C_3}\right) \tag{A15}$$

To recover the shear stress angle, θ, equation A6 is solved for θ with appropriate substitutions for C_1 and β. The result is given in equation A16.

$$\theta = \frac{1}{K_m}\left(\frac{C_1}{\beta} - K_b\right) \tag{A16}$$

The measured normal stress, σ_{meas}, is calculated using the calibration factor from equation A5 and the measured normal bridge output, E_{0C} (see equation A17).

$$\sigma_{meas} = K_{nscf} K_{norm} E_{0C} \tag{A17}$$

The loading angle, ϕ, is calculated by the ratio of the measured normal stress to the measured shear stress as shown in equation A18.

$$\phi = \tan^{-1} \frac{\sigma_{meas}}{\tau_{meas}} \tag{A18}$$

A.6 Performance of Data Reduction and Normal and Shear Stress Recuperation

To demonstrate the performance of the methods described in Section A.4 and A.5, the strain data for an applied pure shear of -50 psi (as shown in Figure A2) was used to calculate the derived quantities $E_{0A}+E_{0B}$ and $E_{0A}-E_{0B}$. The shear bridge A output, E_{0sref}, was also obtained from Figure A2. A separate finite element analysis was used to obtain the normal bridge output, E_{0nref}, for an applied pure tension of +50 psi.

When the normalized derived bridge outputs (equations A2 and A3) are plotted and the fitting coefficients are calculated, the results are shown in Figure A5.

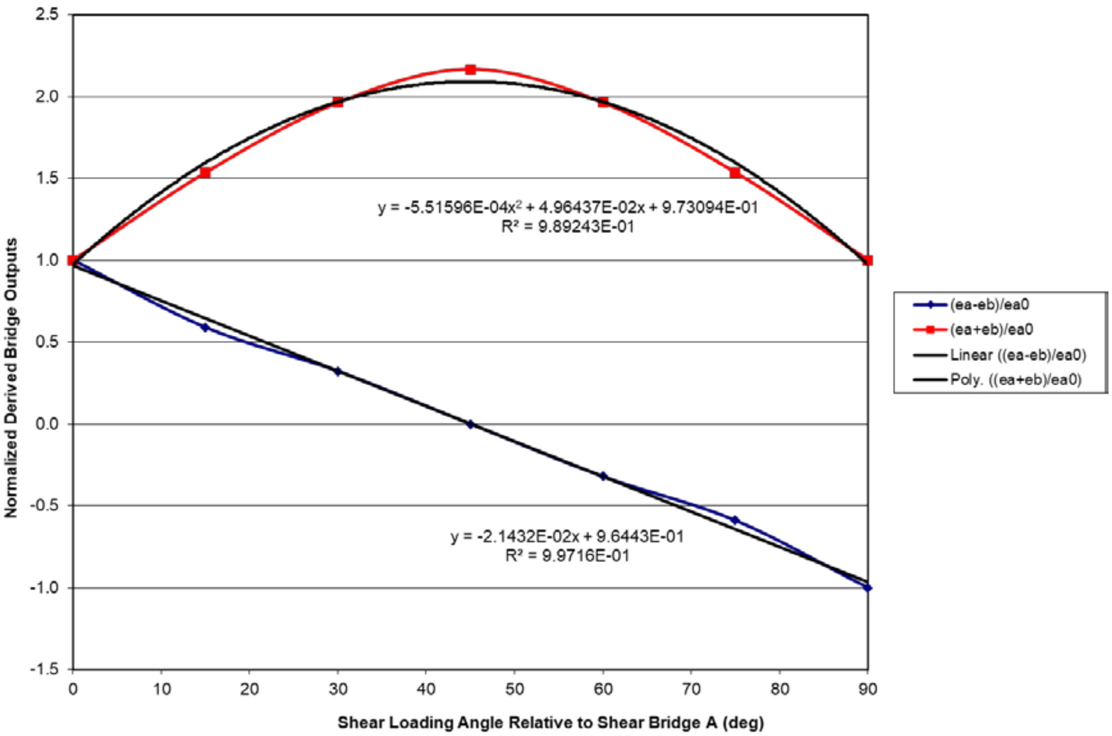

Figure A5. Normalized Derived Bridge Outputs as Function of Shear Loading Angle. Best-fit Linear and Quadratic Trendlines Shown.

Finite element analyses of the calibration device and installed NSST configuration determined that the shear stress concentration factor, K_{sscf}, was 1.2 and the normal stress concentration factor, K_{nscf}, was 0.92.

The performance of the method for the case of a -50 psi pure shear over various shear loading angles is shown in Table A1. Again, these results were generated using the strain data in Figure A2 with equation A1, the fitting coefficients in Figure A5, the aforementioned stress concentration factors and equations A15 and A16.

Table A1. Calculated Stresses and Shear Loading Angle for Pure Shear Loading

Measured Data (mV)		**Calculated (psi, deg, psi)**			**Expected (psi, deg, psi)**			**Error (%diff)**		
ea	eb	appl shear	angle	appl norm	appl shear	angle	appl norm	shear	angle	norm
-9.14E-05	0.00E+00	-51.7	-0.1	-5.6	-50.0	0.0	1.0	3.4	--	-660.0
-9.71E-05	-4.32E-05	-47.3	15.9	-4.0	-50.0	15.0	1.0	-5.4	6.0	-500.0
-1.04E-04	-7.50E-05	-49.9	30.0	-1.8	-50.0	30.0	1.0	-0.2	0.0	-280.0
-9.90E-05	-9.90E-05	-51.8	45.0	0.6	-50.0	45.0	1.0	3.6	0.0	-44.0
-7.50E-05	-1.04E-04	-49.9	60.0	2.3	-50.0	60.0	1.0	-0.2	0.0	130.0
-4.32E-05	-9.71E-05	-47.3	74.1	3.2	-50.0	75.0	1.0	-5.5	-1.2	220.0
0.00E+00	-9.14E-05	-51.7	90.0	3.6	-50.0	90.0	1.0	3.4	0.0	259.0

A fictitious expected applied normal stress of +1 psi was used in Table A1 prevent a divide by zero error from occurring in the percentage error calculations. It can be seen for this loading case that the error in the calculated shear stress ranged from -5.5% to +3.6%. The error in the calculated shear loading angle ranged from -1.2% to +6.0%. The normal stresses ranging from -5.6 psi to +3.6 psi occurred due to apparent increase in radial strain at the diaphragm center as the shear direction changed from 0 deg to 90 deg (see Figure A2).

The performance for a tension-shear load case is shown in Table A2. A +50 psi stress was applied at a loading angle, $\phi = 135$ deg., over shear loading angles of $0 < \theta < 90$ deg. The calculated shear stress error ranged from -1.5% to 10.5% while the calculated shear loading angle error ranged from -1.7% to +8.0%. The calculated normal stress error ranged from -7.9% to +6.8%. Again, an increasing normal stress with shear angle from 0 deg to 90 deg contributes to the normal stress error.

Table A2. Calculated Stresses and Shear Loading Angle for Tension-Shear Loading

Measured Data (mV)		**Calculated (psi, deg, psi)**			**Expected (psi, deg, psi)**			**Error (%diff)**		
EA	EB	appl shear	angle	appl norm	appl shear	angle	appl norm	shear	angle	norm
-6.92E-05	0.00E+00	-39.1	-0.1	32.6	-35.4	0.0	35.4	10.5	--	-7.9
-7.17E-05	-3.24E-05	-34.9	16.2	33.4	-35.4	15.0	35.4	-1.4	8.0	-5.6
-7.70E-05	-5.63E-05	-36.9	30.7	34.7	-35.4	30.0	35.4	4.2	2.3	-2.0
-7.44E-05	-7.44E-05	-38.9	45.0	36.0	-35.4	45.0	35.4	9.9	0.0	1.7
-5.63E-05	-7.70E-05	-36.9	59.3	37.0	-35.4	60.0	35.4	4.1	-1.2	4.6
-3.24E-05	-7.17E-05	-34.9	73.8	37.5	-35.4	75.0	35.4	-1.5	-1.7	6.0
0.00E+00	-6.92E-05	-39.1	90.1	37.8	-35.4	90.0	35.4	10.5	0.1	6.8

LIST OF ACRONYMS

AMRDEC .	U.S. Aviation and Missile Research Development and Engineering Center
DBST	Dual Bond Stress and Temperature sensor
DIST	Distance
FEA	Finite Element Analysis
NSST	Normal-Shear Stress and Temperature sensor
SRM	Solid Rocket Motor

This page intentionally left blank.